Numerical Evolution of Correlation Functions With Applications to Dynamically Localized Quantum Fields

by

Boris Ragula

A thesis
presented to the University of Waterloo
in fulfillment of the
thesis requirement for the degree of
Master of Mathematics
in
Applied Mathematics

Waterloo, Ontario, Canada, 2024

Author's Declaration

This thesis consists of material all of which I authored or co-authored: see Statement of Contributions included in the thesis. This is a true copy of the thesis, including any required final revisions, as accepted by my examiners.

I understand that my thesis may be made electronically available to the public.

Statement of Contributions

This thesis is based on, and contains results from the following works:

1. **Boris Ragula**, Erik Schnetter, and Eduardo Martín-Martínez, "A finite difference method for numerically evolving correlation functions of scalar quantum fields", (In Preparation) [57];

2. Eduardo Martín-Martínez, **Boris Ragula**, Erik Schnetter, and Bruno de S. L. Torres, "Localizing quantum fields with time-dependent potentials", (In Preparation) [43].

The results of paper (1) appear in Chapter 3, Sec. 3.2, 3.3, 3.4, and all associated subsections. I was the main author responsible for designing and testing the algorithm that is presented. The text is being edited collaboratively by all co-authors.

The results of paper (2) appear in all sections of Chapter 4. I was the main author responsible for creating the plots and numerical methods that were used for obtaining the results of Sec. 4.2 and Sec. 4.3. Bruno de S.L. Torres was responsible for the majority of the calculations in Sec. 4.1, and derivations of the symplectic eigenvalue calculations in Sec. 4.3. The text is being edited collaboratively by all co-authors.

Abstract

This thesis presents two topics at the interface between computational physics and Quantum Field Theory (QFT). This first part of the thesis is a comprehensive study of a numerical evolution scheme for the correlation function of a scalar quantum field. In particular, it explores how one can numerically simulate a bi-scalar function that simultaneously satisfies a time dependent partial differential equation Partial Differential Equations (PDE) in two independent spacetime coordinates. We demonstrate an algorithm that is capable of performing time integration in two time coordinates and yielding convergent numerical results for not only the correlation function, but also for quantities of interest relating to the quantum field. Moreover, we demonstrate a number of methods that can be leveraged to optimize the speed along with the required memory of the algorithm.

The second part of this thesis is concerned with the effects of dynamically localizing the vacuum state of scalar quantum field in $(1+1)$-dimensional Minkowski spacetime. Given recent develops in formulations to a measurement theory for quantum fields, localized field theories have emerged as a potential candidate in developing a relativistically consistent measurement theory. However, concerns have been raised regarding the use of these localized fields in realistic, experimental setups due to the fact that one must dynamically localize the field. The result of this localization would be a loss of purity in the experimentally accessible modes of the field, and thus would not be useful as a measurement device. Utilizing the methods presented in the first part of this thesis, we study the effect of localizing quantum field degrees of freedom by dynamically growing cavity walls through a time-dependent potential. We use our results to show that it is possible to do this without introducing non-negligible mixedness in localized modes of the field. We discuss how this addresses the concerns, raised in previous literature, that the high degree of entanglement of regular states in QFT may hinder relativistic quantum information protocols that make use of localized relativistic probes.

Acknowledgements

I would like to first thank my supervisor, Eduardo Martín-Martínez for his guidance and support throughout my Master's program. His reliability, knowledge, and insight into the theoretical aspects of this research was invaluable to the success and completion of this thesis. I would additionally like to thank Erik Schnetter for sharing his knowledge and enthusiasm regarding the numerical topics of this project.

I want to also thank my research colleagues from the Barrio RQI research group (Erickson, Koji, Jose, Bruno, Rick, Carol, Adam, Kelly, Matheus, and Eirini) for casual conversations during a coffee break, sharing Airbnbs during conferences, crucial discussions about our research, and simply for nights out away from work. I would also like to thank all those in the Geometry Forge research group (Conner, Stamatis, Alex, Lucas, and Annamalai) for all their discussions and incredible knowledge that they shared with me regarding numerics, and for lunches at Perimeter Institute where we could all relax with good food and friends.

I want to give a special thank you to all of my friends back home (Grey, Joseph, and Krista) for always supporting me when I needed it most, and always making the time to see each other during the few vacations where I could go home and see you. A huge thanks to all the friends I have made while I've been here (Taran, Zac, Salman, Mike, Matt, Claudia, Lori, Jay, Lauren, Mila, and Pieter) for continually being by my side. You have all made Waterloo truly feel like home be it through movie nights, visiting Niagara, or just chatting in the living room.

I can't express enough gratitude and will always be thankful to my parents and my brother for supporting me endlessly throughout my entire academic career. Their encouragement will forever be a driving force that allows me to be the person I am today. To my aunts, uncles and cousins, thank you for always being supportive, spending holidays together, getting together for a football game, and just spending time together whenever possible.

Lastly, and far from least, I would like to thank my loving partner Carlee for having my back day in and day out. Thank you for every dinner date, every vacation, every holiday, and each day that you put a smile on my face. This path would have been significantly more difficult without you, and you have given me some of the best memories during my Master's journey.

Throughout this thesis I was supported through the Queen Elizabeth II Graduate Scholarship in Science and Technology, along with the Ontario Graduate Scholarship.

Table of Contents

List of Figures

List of Abbreviations

CCR canonical commutation relations 6, 7, 9

CFL Courant-Friedrichs-Lewy 15, 17

FD Finite Difference 2, 3, 13–15, 21, 22, 56, 70

PDE Partial Differential Equations iv, 1–3, 13–15, 17, 18, 20, 21

QFT Quantum Field Theory iv, 1–4, 7–9, 11, 56, 58

RQI Relativistic Quantum Information 2, 3, 10, 57, 58

Notations and Conventions

Spacetime is given by a pair $(\mathcal{M}, g_{\mu\nu})$, where $\mathcal{M}$ is differentiable manifold consisting of one spatial and one temporal coordinate and $g_{\mu\nu}$ is a Lorentzian metric on $\mathcal{M}$. The manifold, $\mathcal{M}$, will always be assumed to be globally hyperbolic in order to ensure the existence of a Cauchy slice. The importance of this assumption will be discussed in more detail in Chapter 3. We will be working in a Cartesian coordinate system $x^\mu = (t, x^1, \ldots, x^n)$ where n is the number of spatial dimensions. Given that we are working in a Minkowski spacetime, the metric and its signature are given by $\eta_{\mu\nu} = \text{diag}(-1, +1, \ldots, +1)$. We will refer to abstract points in spacetime using sans-serif font, x, x'. We use natural units so that $\hbar = c = 1$. In order to clearly distinguish quantum operators from classical quantities, we will always use hats to denote the quantum operators. For example, $\hat{\phi}(\mathsf{x})$ represents the operator associated to the quantized classical field $\phi(\mathsf{x})$.

Chapter 1

Introduction

Quantum field theory (QFT) forms the basis of modern physics, providing a unifying mathematical framework to describe fundamental particles and their interactions. As the foundation of the Standard Model of particle physics, QFT has provided groundbreaking insights into the workings of nature at the most fundamental level. Despite its success in explaining experimental observations, the mathematical complexity of QFT, especially with regards to the PDEs that describe the evolution of these fields, poses significant challenges for analytical and numerical analysis. Numerically simulating the PDEs associated to quantum fields requires a method to avoid working with infinite degrees of freedom, making the process both computationally demanding and conceptually challenging. These intricacies motivate the development of novel numerical techniques and approximations. This thesis addresses some of these challenges, with a particular focus on exploring numerical methods for localized quantum field configurations.

Despite the ubiquity of PDEs in the mathematical description of QFTs, solving PDEs analytically is often impractical or simply intractable, particularly in cases with external driving forces or nonlinear interactions. As a result, numerical methods for PDEs have become indispensable tools, enabling simulations and predictions of physical phenomena with a high degree of accuracy. These methods generally face challenges of ensuring numerical stability, convergence, and managing computational costs associated with high-dimensional problems that require careful algorithm design. Thus, we aim to overcome these challenges to allow for a more efficient study of the intricate and nuanced properties of quantum fields.

With this in mind, the study of scalar QFTs yields intuition about the nature of fundamental physics. Central to many of these studies are the correlation functions, which encode essential information about the quantum dynamics and statistical properties of

the field [19]. However, the numerical evolution of these functions, particularly due to the presence of multiple time variables, presents unique challenges due to the complexity of the governing PDEs. In this paper, we introduce a robust numerical scheme for solving such PDEs, focusing on Finite Difference (FD) methods designed to optimize computational efficiency and memory usage. By balancing precision and computational resources, our approach provides a versatile framework for advancing the study of scalar quantum fields and their applications to increasingly complex systems.

In spite of its successes, QFT continues to face significant challenges that limit its potential as a comprehensive framework for describing all physical phenomena. In particular, for the study of this thesis, localization poses a subtle, yet, unavoidable problem. In particular, it is known that there is no meaningful notion of a "position" operator in relativistic QFTs, nor is it possible to perform finite-rank projective measurements on local subregions of spacetime without incurring problems with causality [59, 62, 29, 58]. This is problematic from the viewpoint of QFT and quantum information theory, as local measurements and operations form the basis of quantum information protocols that are covariant and causal in a relativistic sense.

In order to remedy these subtleties, *particle detectors* have arisen as a versatile tool when dealing with local measurements and operations in QFT. A particle detector is a tool regularly used in the Relativistic Quantum Information (RQI) community and consists of a physically reasonable, localized quantum system that can be used as a probe of a QFT in some local region of spacetime. These types of particle detectors have been used with great success for studying several scenarios in the interface of quantum theory and relativity ranging from the Unruh effect and Hawking radiation [72, 9, 17], to a framework for the measurement theory in QFT [52], to quantum information protocols in relativistic settings that use quantum fields as mediators [13, 36, 64, 33, 6, 73, 60, 63].

In general, the quantum systems used as particle detectors are internally nonrelativistic, due to the close parallel between particle detectors in RQI and physical scenarios in which the systems acting as the probes are accurately described by nonrelativistic quantum mechanics. A paradigmatic example of this is found in the light-matter interaction, where the internal dynamics of the atom (which acts in this context as a probe for the electromagnetic field) is well-approximated by nonrelativistic physics in most of the regimes of interest in atomic physics and quantum optics [39]. These nonrelativistic approximations are well-justified in many scenarios; however, it has been noted that internally nonrelativistic systems as probes can result in violations of relativistic causality and covariance when the spatial distribution of the probes is not pointlike [42, 14]. This has led to renewed interest in particle detector models that are described by quantum fields as a way of reconciling probe models with the causal and covariant framework of QFT [21, 22, 46, 49].

The feasibility of fully relativistic local field modes as probes for quantum information protocols has recently been put into question in the context of entanglement harvesting, which is a protocol to extract entanglement from quantum field degrees of freedom in two spacelike separated regions [54, 51, 53, 55, 23, 44, 30]. It has been pointed out that, at a fundamental level, the restriction of the state of a QFT to a subset of degrees of freedom on a finite subregion will inevitably result in a mixed state. This is a rather general consequence of the Reeh-Schlieder theorem, as recently studied in [49, 71, 48].

In this thesis, we will investigate to what degree the resulting localized field can be used to produce truly local modes of the field in a highly pure state when the localization profile of the field is implemented through dynamical external potentials. In particular, we will investigate to what degree the resulting localized field can be used to produce truly local modes of the field in a highly pure state. This is of importance when using localized quantum fields as probes for RQI protocols, as it has been shown that mixedness of a probe inhibits how much vacuum entanglement can be extracted by detectors that are weakly coupled to a quantum field [61, 28]. By localizing a free field through a time-dependent confining potential, we will show it is possible to control to what extent the pure state of the vacuum becomes mixed with respect to the normal modes of the effective cavity that is implemented by the external potential and that in the adiabatic limit (which in practice is most of the regimes where detectors are implemented) the mixedness becomes negligible.

The organization of this thesis is as follows: in Chapter 2 we will provide a textbook review of the necessary techniques and formalism of QFT both in free space and in a cavity, along with a review of the associated correlation function. In Chapter 3 we will give an overview of the FD method for solving the wave equation in $(1+1)$ dimensions and the definition and importance of stability and convergence of PDEs. From there, we give the numerical method designed to solve for the correlation function of a scalar quantum field, the results of our convergence testing, and examples. We also provide a way of numerically obtaining the energy density of scalar quantum fields through the numerically approximated correlation function. In Chapter 4, we extend the methods presented in Chapter 3 to the case of a free scalar quantum field that is localized through the use of an external confining potential. With this, we study the effects of such a localization on the energy density as well as the purity of the normal modes of the dynamically created cavity. Finally, in Chapter 5 we summarize the important results of this thesis and the implications these results have in QFT with particular applications to the field of RQI. We conclude the thesis by providing a brief overview of the applications that can be studied with the techniques that have been built throughout the work on this thesis.

Chapter 2

Scalar Quantum Field Theory

In this chapter, we review the formalism of scalar QFT in an $(n+1)$-dimensional Minkowski spacetime. In doing so, we present the canonical quantization procedure used to obtain a quantum field from a classical field theory. We additionally discuss how one relates a free quantum field to a quantum field in a cavity. From this, we will then derive expressions for the correlation function of a scalar quantum field in both cases, which will be an important focus in the following chapters.

2.1 Canonical Quantization of the Classical Scalar Field

In this section, we will present the standard formalism of the canonical quantization scheme necessary to obtain a scalar quantum field from a classical field theory in $(n+1)$-dimensional Minkowski spacetime (see, e.g. [5, 77]). In doing so, we introduce the creation and annihilation operators, from which we can construct the Hilbert space of our quantum field.

The canonical quantization scheme begins by first considering a scalar field $\phi(x)$ in $(n+1)$-dimensions, where we use the not. The classical scalar field is then described by the action

$$S = -\frac{1}{2}\int \mathrm{d}\mathsf{x}\left(\partial_\mu\phi(\mathsf{x})\partial^\mu\phi(\mathsf{x}) - m^2\phi^2(\mathsf{x})\right), \tag{2.1}$$

where m is the mass of the field, $\phi(\mathsf{x})$. One may then derive the corresponding equation of motion for this classical field through the Euler-Lagrange equations and obtain the following

$$(\Box - m^2)\phi(\mathsf{x}) = 0, \tag{2.2}$$

where $\Box = \partial_\mu \partial^\mu$ is the d'Alembert operator, or wave operator. A general solution to Eq. (2.2) can be written as

$$\phi(\mathsf{x}) = \sum_j \left(a_j u_j(\mathsf{x}) + a_j^* u_j^*(\mathsf{x}) \right), \tag{2.3}$$

for a set $\{u_j(\mathsf{x})\}$ of complex basis solutions. In particular, what we have is a Klein-Gordon field of mass m allowing one to choose this set of basis functions to be *plane waves*. These plane waves can be labeled by their wave vector $\boldsymbol{k}$, and written as

$$u_{\boldsymbol{k}}(\mathsf{x}) \propto e^{\mathrm{i} k_\mu x^\mu}, \tag{2.4}$$

where $k^\mu = (\omega_{\boldsymbol{k}}, \boldsymbol{k})$, and $\omega_{\boldsymbol{k}}$ is given by the dispersion relation

$$\omega_{\boldsymbol{k}} = \sqrt{|\boldsymbol{k}|^2 + m^2}. \tag{2.5}$$

In a free field theory, the wave vector $\boldsymbol{k}$ that is used to label the mode functions is continuous. As a result, the sum over discrete mode functions indexed by j in Eq. (2.3) is instead replaced with an integral over $\boldsymbol{k}$ so that our general solution is now

$$\phi(\mathsf{x}) = \int \mathrm{d}^n \boldsymbol{k} \left(a_{\boldsymbol{k}} u_{\boldsymbol{k}}(\mathsf{x}) + a_{\boldsymbol{k}}^* u_{\boldsymbol{k}}^*(\mathsf{x}) \right). \tag{2.6}$$

One may define the current density of the Klein-Gordon field as

$$J^\mu = \mathrm{i} \left(\phi^*(\mathsf{x}) \partial^\mu \phi(\mathsf{x}) - \partial^\mu \phi^*(\mathsf{x}) \phi(\mathsf{x}) \right), \tag{2.7}$$

which is a vector field satisfying

$$\partial_\mu J^\mu = 0. \tag{2.8}$$

This conserved quantity is useful in defining an inner product for the solution space of Eq. (2.2), known as the Klein-Gordon inner product. The Klein-Gordon inner product is defined to be

$$(f_1, f_2)_{\text{K.G.}} = \mathrm{i} \int_{\Sigma_t} \mathrm{d}^n \boldsymbol{x} \left(f_1^* \partial_t f_2 - f_2 \partial_t f_1^* \right), \tag{2.9}$$

where Σ_t is a codimension-1 surface given by a constant t coordinate in a given inertial reference frame. This surface, known as a *Cauchy slice*, is a particular choice of spatial foliation (equal time t) of the spacetime that ensures a well-posed initial value problem [1].

Using the Klein-Gordon inner product, we impose the following conditions on our set

of basis functions $\{u_{\boldsymbol{k}}(\mathsf{x})\}$

$$(u_{\boldsymbol{k}}, u_{\boldsymbol{k}'})_{\text{K.G.}} = -(u^*_{\boldsymbol{k}}, u^*_{\boldsymbol{k}'})_{\text{K.G.}} = \delta(\boldsymbol{k} - \boldsymbol{k}'), \tag{2.10}$$

$$(u_{\boldsymbol{k}}, u^*_{\boldsymbol{k}'})_{\text{K.G.}} = (u^*_{\boldsymbol{k}}, u_{\boldsymbol{k}'})_{\text{K.G.}} = 0, \tag{2.11}$$

where $\delta(\boldsymbol{k})$ is the Dirac-Delta function. Under these conditions, we arrive at the following expression for the plane wave basis functions

$$u_{\boldsymbol{k}}(\mathsf{x}) = \frac{1}{\sqrt{(2\pi)^n 2\omega_{\boldsymbol{k}}}} e^{\mathrm{i}k_\mu x^\mu}. \tag{2.12}$$

We now want to upgrade the classical field theory of Eq. (2.1) to a quantum field theory. To do so, we assume the field $\phi(\mathsf{x})$ becomes an operator-valued distribution, $\hat{\phi}(\mathsf{x})$, that satisfies the equal time commutation relations given by

$$\left[\hat{\phi}(t, \boldsymbol{x}), \hat{\phi}(t, \boldsymbol{x}')\right] = 0, \tag{2.13}$$

$$[\hat{\pi}(t, \boldsymbol{x}), \hat{\pi}(t, \boldsymbol{x}')] = 0, \tag{2.14}$$

$$\left[\hat{\phi}(t, \boldsymbol{x}), \hat{\pi}(t, \boldsymbol{x}')\right] = \mathrm{i}\delta(\boldsymbol{x} - \boldsymbol{x}'), \tag{2.15}$$

where $\hat{\pi}(\mathsf{x}) = \partial_t \hat{\phi}(\mathsf{x})$ is the canonical conjugate of the field. Additionally, we promote the coefficients, $a_{\boldsymbol{k}}$ and $a^*_{\boldsymbol{k}}$, of the general solution in Eq. (2.6) to the operators $\hat{a}_{\boldsymbol{k}}$ and $\hat{a}^\dagger_{\boldsymbol{k}}$. Thus, our quantum field can be written as a mode decomposition, similar to that of the classical scalar field, as

$$\hat{\phi}(\mathsf{x}) = \frac{1}{(2\pi)^{3/2}} \int \frac{\mathrm{d}^3\boldsymbol{k}}{\sqrt{2\omega_{\boldsymbol{k}}}} (\hat{a}_{\boldsymbol{k}} e^{\mathrm{i}\mathsf{k}\cdot\mathsf{x}} + \hat{a}^\dagger_{\boldsymbol{k}} e^{-\mathrm{i}\mathsf{k}\cdot\mathsf{x}}). \tag{2.16}$$

By imposing the equal time commutation relations of Eqs. (2.13), (2.14), and (2.15), one can show (see. Appendix A) that the operators $\hat{a}_{\boldsymbol{k}}$ and $\hat{a}^\dagger_{\boldsymbol{k}}$ satisfy the following commutation relations, known as the canonical commutation relations (CCR)

$$[\hat{a}_{\boldsymbol{k}}, \hat{a}_{\boldsymbol{k}'}] = 0, \tag{2.17}$$

$$\left[\hat{a}^\dagger_{\boldsymbol{k}}, \hat{a}^\dagger_{\boldsymbol{k}'}\right] = 0 \tag{2.18}$$

$$\left[\hat{a}_{\boldsymbol{k}}, \hat{a}^\dagger_{\boldsymbol{k}'}\right] = \delta(\boldsymbol{k} - \boldsymbol{k}')\mathbb{1}, . \tag{2.19}$$

Following this quantization, we interpret the operators $\hat{a}_{\boldsymbol{k}}$ and $\hat{a}^\dagger_{\boldsymbol{k}}$ seen in the Fourier decomposition of Eq. (2.16) as creation and annihilation operators with a spatial dependence given by the mode functions $u_{\boldsymbol{k}}(\mathsf{x})$. The final step of the canonical quantization procedure is to construct the Hilbert space of the quantum field. In order to so, we begin with a normalized vacuum state $|0\rangle$ which is chosen in such a way that it is annihilated by all annihilation operators,

$$\hat{a}_{\boldsymbol{k}} |0\rangle = 0 \ \ \forall \boldsymbol{k}. \tag{2.20}$$

The Hilbert space of the QFT is defined to be the span of all states obtained through repeated applications of the creation operators on $|0\rangle$. A state is known as a *one-particle state of momentum* $\boldsymbol{k}$ if it is obtained by a single application of the creation operator $\hat{a}^\dagger_{\boldsymbol{k}}$, and is denoted

$$\hat{a}^\dagger_{\boldsymbol{k}} |0\rangle = |1_{\boldsymbol{k}}\rangle \, . \tag{2.21}$$

Similarly, many-particle states may be defined by applications of creation operators with different momenta. This basis of particle states is known as the *Fock basis*.

The states in the Fock basis form an orthonormal basis for the Hilbert space of the quantum field. In the Fock basis, states of different particle number are orthonormal in the sense that $\langle m_{\boldsymbol{k}} | n_{\boldsymbol{k}} \rangle = \delta_{nm}$, where δ_{nm} is the Kroenecker Delta. Additionally, in the simplest case, we can demonstrate the orthonormality of states with different momenta by considering the inner product between two one-particle states, as follows

$$\langle 1_{\boldsymbol{k}} | 1_{\boldsymbol{k}'} \rangle = \langle 0 | \, \hat{a}_{\boldsymbol{k}} \hat{a}^\dagger_{\boldsymbol{k}'} \, |0\rangle = \langle 0 | \left(\delta(\boldsymbol{k} - \boldsymbol{k}') + \hat{a}^\dagger_{\boldsymbol{k}'} \hat{a}_{\boldsymbol{k}} \right) |0\rangle = \delta(\boldsymbol{k} - \boldsymbol{k}'), \tag{2.22}$$

where in the second equality we have used the CCR in Eq. (2.19), and in the third equality we used the fact that the vacuum is normalized and annihilated by all creation operators. These two properties can be used to derive the orthogonality condition between any two Fock states. In what follows, we will use the results of the canonical quantization procedure to construct a cavity QFT.

2.2 Quantum Field Theory in a Cavity

Given the canonical quantization procedure for a free field theory, we now demonstrate how one can derive similar results for a scalar quantum field confined to a cavity. This will be particularly important for the numerical methods that will be used in future sections. In order to achieve this, we first assume that our field is confined to a box of width L, that satisfies Dirichlet boundary conditions. Specifically, we assume the field is exactly zero at

the boundary. As was shown in Sec. 2.1, the basis solutions to the scalar wave equation is given by

$$u_{\boldsymbol{k}} = \alpha e^{\mathrm{i}\mathsf{k}\cdot\mathsf{x}}, \tag{2.23}$$

where α is some normalization constant.

In order to ensure that our QFT satisfies the boundary conditions of the cavity, $\phi(t,0) = \phi(t,L) = 0$, we can simply impose the boundary conditions on the basis functions themselves. That is

$$u_{\boldsymbol{k}}(t,0) = \alpha\left(A\cos(0) + B\sin(0)\right)e^{-\mathrm{i}kt} = 0 \implies A = 0, \tag{2.24}$$

$$u_{\boldsymbol{k}}(t,L) = \alpha B\sin(kL)e^{-\mathrm{i}kt} = 0 \implies k_n = \frac{n\pi}{L}. \tag{2.25}$$

This leads to our basis solutions being given by

$$u_{k_n}(t,x) = \alpha_n \sin(k_n x)e^{-\mathrm{i}k_n t}. \tag{2.26}$$

Now, we must also ensure that each of the basis functions are normalized under the Klein-Gordon inner product in Eq. (2.9). Specifically, we find that

$$(u_{k_n}, u_{k_n})_{\text{K.G.}} = 1 \implies \alpha_n = \frac{1}{\sqrt{n\pi}}. \tag{2.27}$$

This yields a general solution for our cavity field given by

$$\phi(t,x) = \sum_n \frac{1}{\sqrt{n\pi}}\left(a_{k_n}\sin(k_n x)e^{-\mathrm{i}k_n t} + a^*_{k_n}\sin(k_n x)e^{\mathrm{i}k_n t}\right). \tag{2.28}$$

We then follow the procedure outlined in Sec. 2.1 to quantize the field and we arrive at the following expression for our quantum field in a cavity

$$\hat{\phi}(x,t) = \sum_n \frac{1}{\sqrt{n\pi}}\left(\hat{a}_{k_n}\sin(k_n x)e^{-\mathrm{i}k_n t} + \hat{a}^\dagger_{k_n}\sin(k_n x)e^{\mathrm{i}k_n t}\right). \tag{2.29}$$

Similarly to the free field case, the equal time commutation relations in Eqs. (2.13),(2.14), and (2.15) result in the canonical commutation relations for our quantum field in a cavity.

In particular these are given by

$$[\hat{a}_{k_n}, \hat{a}_{k_m}] = 0, \tag{2.30}$$

$$\left[\hat{a}^\dagger_{k_n}, \hat{a}^\dagger_{k_m}\right] = 0, \tag{2.31}$$

$$\left[\hat{a}_{k_n}, \hat{a}^\dagger_{k_m}\right] = \delta_{nm}\mathbb{1}. \tag{2.32}$$

We notice that, overall, the solutions in the cavity and free space are quite similar. The main difference is in the labels used for the momenta. In free space, the wave vector $\boldsymbol{k}$ labeling different mode functions is continuous, which results in the solution for our quantum field being an integral over $\boldsymbol{k}$ and the CCRs contain Dirac deltas. In the cavity case, we have a sum over discrete momenta and our solution is a sum over n and the CCRs contain Kronecker deltas.

2.3 The Correlation Function

In this review section, we will focus our attention on the two-point correlator, or correlation function, of the field. We will review its definition, its relevance for the purpose of this thesis, and its explicit form in a few relevant cases. Additionally, we lay out the time evolution equations for the two-point function which will be critical to the numerical approach employed in the next chapter.

2.3.1 Generalities of the Two-Point Function

Given a quantum scalar field $\hat{\phi}(\mathsf{x})$ in a state $\hat{\rho} = |\psi\rangle\langle\psi|$, the two-point function is given by

$$W(\mathsf{x}, \mathsf{x}') = \langle\hat{\phi}(\mathsf{x})\hat{\phi}(\mathsf{x}')\rangle_{\hat{\rho}} = \mathrm{Tr}\left(\hat{\rho}\hat{\phi}(\mathsf{x})\hat{\phi}(\mathsf{x}')\right), \tag{2.33}$$

where x and x' are two arbitrary spacetime points.

The two-point function plays a crucial role in many aspects of QFT. If the state $\hat{\rho}$ is Gaussian with vanishing first moments - as is the case of the vacuum as well as any squeezed thermal state of a theory with linear equations of motion - then all information about the quantum state $\hat{\rho}$ is encoded in $W(\mathsf{x}, \mathsf{x}')$. This allows for a much more efficient description of the physics of Gaussian states through properties of the two-point function [65, 67, 66]. Moreover, even if $\hat{\rho}$ is not Gaussian, the two-point function contains all the information

needed to specify the stress-energy tensor of a field theory with a quadratic action such as the theory in Eq. (2.1) [5, 74]. Finally, the two-point function fully determines the leading-order response of the system to the action of an external agent that is linearly coupled to the quantum field. This has applications in the linear response theory of the quantum field under the influence of external sources, and also characterizes the leading-order effect of the field on the state of localized probes that couple to it - for instance, in the context of particle detectors in RQI [17, 40, 13, 41, 36, 64, 70].

Given the definition of the correlation function in Eq. (2.33), and the fact that our field $\hat{\phi}$ satisfies the wave equation, it is possible to show that the correlation function satisfies

$$\begin{aligned}(\partial_t^2 - \partial_x^2)W(\mathsf{x},\mathsf{x}') = 0,\\ (\partial_{t'}^2 - \partial_{x'}^2)W(\mathsf{x},\mathsf{x}') = 0.\end{aligned} \tag{2.34}$$

Given its importance, it is useful to have explicit forms for the two-point function in a variety of situations. If we take the field state to be given by $\hat{\rho} = |0\rangle\langle 0|$, where we recall that $|0\rangle$ is defined as the state annihilated by all annihilation operators $\hat{a}_{\boldsymbol{k}}$, then we have

$$W_0(\mathsf{x},\mathsf{x}') = \int \mathrm{d}^n\boldsymbol{k} u_{\boldsymbol{k}}(\mathsf{x})u^*_{\boldsymbol{k}}(\mathsf{x}'). \tag{2.35}$$

For a scalar field in free space with $m^2 = \text{const.}$, we can use the mode functions in terms of plane waves as given in Eq. (2.12) to find

$$W_0(\mathsf{x},\mathsf{x}') = \int \frac{\mathrm{d}^n\boldsymbol{k}}{(2\pi)^n 2\omega_{\boldsymbol{k}}} e^{\mathrm{i}k_\mu(x-x')^\mu}, \tag{2.36}$$

where a full derivation of this expression is given in Appendix A.

Another ubiquitous example is that of a one-particle Fock state, which is a natural way to construct wavepackets of the field that are initially localized in space. These states are generally of the form

$$|\psi\rangle = \int \mathrm{d}^n\boldsymbol{k} f(\boldsymbol{k})\hat{a}^\dagger_{\boldsymbol{k}}|0\rangle\,, \tag{2.37}$$

where

$$\int \mathrm{d}\boldsymbol{k}|f(\boldsymbol{k})|^2 = 1, \tag{2.38}$$

and $f(\boldsymbol{k})$ is the spacetime localization profile of the field. For this state, the two-point function becomes

$$W_\psi(\mathsf{x},\mathsf{x}') = h(\mathsf{x},\mathsf{x}') + W_0(\mathsf{x},\mathsf{x}'), \tag{2.39}$$

where

$$h(\mathsf{x},\mathsf{x}') = F(\mathsf{x})F^*(\mathsf{x}') + F^*(\mathsf{x})F(\mathsf{x}') \tag{2.40}$$

is the state-dependent component of the two-point function, and

$$F(\mathsf{x}) = \int \mathrm{d}\boldsymbol{k} f(\boldsymbol{k}) u_{\boldsymbol{k}}(\mathsf{x}). \tag{2.41}$$

More generally, it is possible to show that for any Hadamard state $|\psi\rangle$ in the Hilbert space of the QFT, which will be the case for all states investigated throughout this thesis, the two-point function will be given by an expression similar to Eq. (2.39), where $h(\mathsf{x},\mathsf{x}')$ will have a different form depending on the choice of $|\psi\rangle$ e.g. [47, 25, 35, 20].

2.3.2 Example in a Cavity

Given that the underlying goals of this thesis are to present a numerical evolution scheme for the two-point function, and use this method to study the effects of a confining potential on the dynamics of an otherwise free quantum field, it is instructive to review some basic features of the two-point function in a cavity. This is because a cavity is nothing more than an idealized version of a confining potential that perfectly traps the quantum field in a finite spatial region. Moreover, as will be seen in Chapter 3, our numerical methods will inevitably rely on calculations in a finite computational domain. This requires us to specify how we treat the system degrees of freedom at the boundaries of the domain, which ultimately acts as an effective cavity in its own right.

In this Section and for the rest of this paper, we will restrict ourselves to the case of a scalar quantum field in $(1+1)$-dimensional Minkowski spacetime. The field is then defined to be restricted within the region of given by $0 \leq x \leq L$, where L is the total length of the cavity as was done in Sec. 2.2. Moreover, we can replace the free space mode solutions by those of cavity mode solutions and replacing all integrals over $\boldsymbol{k}$ with sums over n in Eq. (2.35) to obtain the following solutions for the vacuum correlation function in the cavity

$$W_0(\mathsf{x},\mathsf{x}') = \frac{1}{\pi}\sum_n \frac{1}{n}\sin(k_n x)\sin(k_n x')e^{-\mathrm{i}k_n(t-t')}. \tag{2.42}$$

By following a similar approach to the previous section, and making the appropriate substitutions to account for the discreteness of the modes in the cavity, we may construct

a Fock wavepacket as

$$|\psi\rangle = \sum_{n=1}^{\infty} f(n)\hat{a}^{\dagger}_{k_n} |0\rangle \,, \tag{2.43}$$

where $f(n)$ must be chosen such that

$$\sum_{n=1}^{\infty} |f(n)|^2 = 1. \tag{2.44}$$

Here we can see that Eqs. (2.43) and (2.44) are the cavity analogues to Eqs. (2.37) and (2.38), respectively. Given this one-particle state, the resulting cavity two-point function is then

$$W_{\psi}(\mathsf{x}, \mathsf{x}') = F^*(\mathsf{x})F(\mathsf{x}') + F(\mathsf{x})F^*(\mathsf{x}') + W_0(\mathsf{x}, \mathsf{x}'), \tag{2.45}$$

where

$$F(\mathsf{x}) = \sum_{n=1}^{\infty} \frac{f(n)}{\sqrt{n\pi}} \sin(k_n x) e^{-\mathrm{i}k_n t}. \tag{2.46}$$

In both the continuum and cavity case, we see that the state dependent component of the two-point function can be described through an integral transformation of the momentum profile for the state of interest. Additionally, the boundary conditions can introduce inhomogeneities in the spatial distribution of the modes. It is precisely the dynamics of Eq. (2.45) that we will study with our numerical methods.

Chapter 3

Numerical Methods

In this chapter, we present a brief review of FD methods for simulating time-dependent PDEs, along with a review of stability and convergence for numerical methods. We then demonstrate the numerical method used to evolve correlation functions and how one can obtain the energy density from these simulations. Additionally, throughout this chapter, we will be working in $(1+1)$-dimensional Minkowski spacetime. We note that all simulations and plots were generated using the Julia programming language [4], along with the packages in [7, 10].

3.1 Numerical Partial Differential Equations

In this section, we will present a textbook review of how one can simulate time-dependent PDEs on a computer [38, 45, 69]. In particular, we will focus on the scalar wave equation as this will create the foundations necessary to simulate the evolution of the correlation function in Section 3.2. We also investigate the stability and convergence of hyperbolic PDEs, as this is essential in verifying the effectiveness and accuracy of a given numerical method.

3.1.1 Finite Difference Method For the Classical Scalar Field

Let us first look at the case of a massless classical scalar wave equation in (1+1)-dimensional Minkowski spacetime. The massless scalar field satisfies the following equation of motion

$$(\partial_t^2 - \partial_x^2)\phi(t,x) = 0, \tag{3.1}$$

where we have explicitly written the d'Alembert operator, $\Box = \partial_\mu \partial^\mu$. We assume that our field is confined within a spatial domain $\Omega_x = [0, L]$, where $L > 0$, and that we will evolve the system for a finite time T, so that our temporal domain is $\Omega_t = [0, T]$.

The guiding principle of the FD method is to then approximate the solution of Eq. (3.1) at a set of discrete points in the simulation domain, $\Omega = [0, L] \times [0, T]$. In order to do this, we first discretize the spatial domain into a set of evenly spaced points, known as *grid points*, $\{x_i\}_{i=0}^{N_x}$ whose separation is $\Delta x = x_i - x_{i-1}$. Similarly, we discretize our temporal domain by a set of grid points $\{t_n\}_{n=0}^{N_t}$, where the number of grid points in time does not necessarily equal the number of grid points in space, and the grid spacing is again given by $\Delta t = t_n - t_{n-1}$. In Fig. 3.1, we show a visualization of the discretization for the spatial and temporal domains. Finally, we adopt the notation that $\phi_i^n \approx \phi(t_n, x_i)$, that is, ϕ_i^n is an approximate solution to the equation of motion at every grid point.

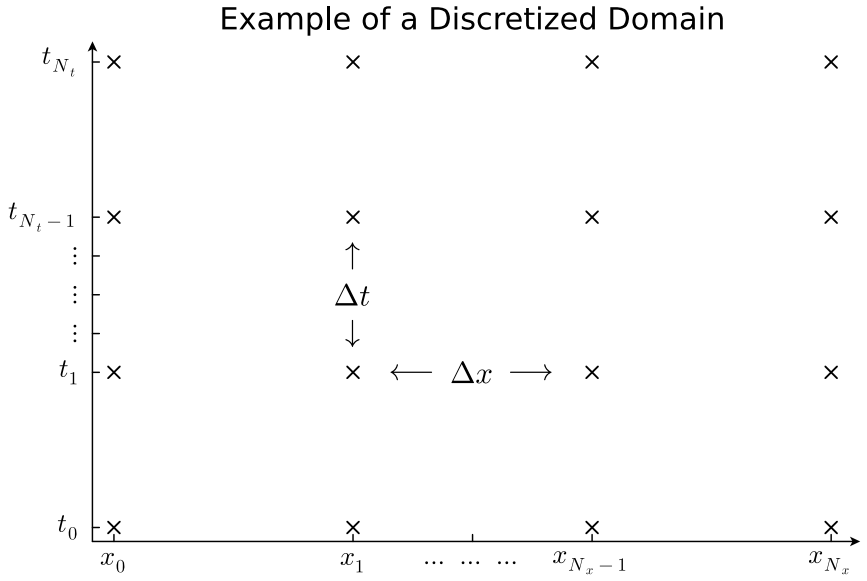

Figure 3.1: This plot demonstrates how one can visualize the discretization of the spatial and temporal domains. Each marker represents the point in the domain where the function $\phi(t, x)$ will be approximated.

Given the grid structure for the domain of our PDE, we now turn our attention to how one can simulate the dynamics of the wave equation on this grid. First, one must construct discrete derivatives that act on our function at each grid point. For example, we

can choose a 2nd order FD stencil for the second derivative in space given by

$$[D_x^2 f]_i^n = \frac{1}{\Delta x^2}\left(f_{i+1}^n - 2f_i^n + f_{i-1}^n\right), \tag{3.2}$$

where we use the notation $[D_\mu^k f]_i^n$ to represent the discrete k^{th} derivative in the coordinate direction $\mu = t, x$ of a function $f(t, x)$ at the grid point (x_i, t_n). This stencil can be derived by performing a Taylor expansion on ϕ_{i+1}^n and ϕ_{i-1}^n around the point ϕ_i^n [38, 37]. If one wanted a higher order stencil, more terms of the form $\phi_{i\pm j}^n$ would be needed to find the grid points necessary to construct the stencil [3]. Thus, to approximate the spatial derivative for our field ϕ, we have

$$[D_x^2 \phi]_i^n \approx \partial_x^2 \phi(x_i, t_n). \tag{3.3}$$

With the discrete derivative operators of the form Eq. (3.2), and an analogous expression for the temporal derivative, we can write down a fully discretized version of Eq. (3.1) as follows

$$\frac{1}{\Delta t^2}\left(\phi_i^{n+1} - 2\phi_i^n + \phi_i^{n-1}\right) - \frac{1}{\Delta x^2}\left(\phi_{i+1}^n - 2\phi_i^n + \phi_{i-1}^n\right) = 0. \tag{3.4}$$

Importantly, this gives us a method in which we can "step" our simulation forward in time. By rearranging Eq. (3.4) for ϕ_i^{n+1}, we can approximate the solution to our function at a new temporal grid point by using the grid data from the previous two time steps. That is,

$$\phi_i^{n+1} = 2\phi_i^n - \phi_i^{n-1} + C^2\left(\phi_{i+1}^n - 2\phi_i^n + \phi_{i-1}^n\right), \tag{3.5}$$

where $C = \frac{\Delta t}{\Delta x}$ is the Courant-Friedrichs-Lewy (CFL) factor, which plays an important role when discussing the stability of a numerical method in Sec. 3.1.2. We can then recursively solve for an approximate solution to our equation of motion by recursively evaluating Eq. (3.5) at every grid point in both time and space.

In addition to the equation of motion, our PDE also has the requirement of two initial conditions and, due to the finite domain, two boundary conditions that must be imposed. In this case, we assume that the initial conditions for our field will be given by

$$\phi(0, x) = f(x), \tag{3.6}$$
$$\partial_t \phi(0, x) = g(x), \tag{3.7}$$

where $f, g \in C^\infty(\Omega)$, $f(x)$ represents the initial field configuration and $g(x)$ represents the initial momentum of the field. Moreover, we will assume that the boundary conditions are

given by Dirichlet boundary conditions so that

$$\phi(t,0) = \phi(t,L) = 0, \tag{3.8}$$

which is a common choice in field theories, representing fields that have no allowed fluctuations at the boundary and can be achieved by simply setting $\phi_0^n = \phi_{N_x}^n = 0$. Additionally, we also have to represent the initial conditions on our grid and do so by choosing the following discrete 2^{nd} order first derivative operator given by

$$[D_t f]_i^n = \frac{1}{2\Delta t}\left(f_i^{n+1} - f_i^{n-1}\right), \tag{3.9}$$

which yields the following discrete analog of our initial conditions

$$\phi_i^0 = f_i \tag{3.10}$$

$$\frac{1}{2\Delta t}\left(\phi_i^1 - \phi_i^{-1}\right) = g_i. \tag{3.11}$$

In Eq. (3.11) we notice the term ϕ_i^{-1}, which leads one to believe they must have grid data from "before" the initial conditions were provided ($n = 0$).

We can address the problem in Eq. (3.11) by noticing that at the first time step in Eq. (3.5) we have

$$\phi_i^1 = 2\phi_i^0 - \phi_i^{-1} + C^2\left(\phi_{i+1}^0 - 2\phi_i^0 + \phi_{i-1}^0\right), \tag{3.12}$$

which also contains a ϕ_i^{-1} term. If we rearrange Eq. (3.11) to solve for the ϕ_i^{-1} term, we can substitute this into Eq. (3.12) and write our first time step in terms of the given initial condition. Explicitly, the first time step is then given by

$$\phi_i^1 = \phi_i^0 + \Delta t g_i + \frac{1}{2}C^2\left(\phi_{i+1}^0 - 2\phi_i^0 + \phi_{i-1}^0\right). \tag{3.13}$$

With Eqs. (3.5) and (3.13), we can generate an approximate solution to the wave equation with initial conditions given by Eqs. (3.6) and (3.7). With this method, we can now proceed to review the concepts of stability and convergence in numerical methods.

3.1.2 Stability and Convergence

Given a numerical method, it is important to test the reliability of the approximation. In particular, we first want a way to validate the *stability* of the method. This is directly related to ensuring that any errors will not propagate and grow unboundedly over long

simulation times, or equivalently over many time steps. To study the stability of our method, we first define the error of a numerical method, which is given by

$$e_i^n = \tilde{\phi}_i^n - \phi_i^n, \tag{3.14}$$

where $\tilde{\phi}_i^n = \phi(t_n, x_i)$ is the exact solution to the PDE and ϕ_i^n is the numerical approximation obtained by the method. A numerical method is said to be *stable* if the error, e_i^n, is bounded as $n \to \infty$ [2].

One common method to determine the stability conditions for a particular numerical scheme is through *Von Neumann stability analysis*. This analysis begins by decomposing the error into a Fourier series at each time step. Specifically, we have

$$e_j^n = \hat{e}_n e^{\mathrm{i}kx_j}, \tag{3.15}$$

where k is the wavenumber of a particular Fourier mode, and $x_j = j\Delta x$, since we are working with a uniform grid. In particular, a necessary condition for a method to be stable is that

$$\left| \frac{\hat{e}_{n+1}}{\hat{e}_n} \right| \leq 1 \ \ \forall k. \tag{3.16}$$

Intuitively, this means that we must choose our time step to be proportional to the highest frequency mode to ensure that information is not gained from points outside the domain of dependence. Given that the spatial derivative depends only on three neighboring grid points from the previous time step, we must demand that the time step is "small enough" to ensure that no information from any other grid points can reach the new point of interest. In particular, "small enough" is determined by the particular numerical method that is chosen. In our case, a von Neumann stability analysis of the wave equation with 2nd order discrete derivatives in both time and space results in a stability condition given by

$$\Delta t \leq \Delta x \tag{3.17}$$

or, more simply, the CFL factor must be less than or equal to one. For the general Klein-Gordon equation, if a mass term is present, then the CFL factor will necessarily change to account for the mass of the field, and as we will see in the case of dynamic localization, will depend on external driving forces.

In addition to stability, one wants to ensure the accuracy of a numerical method as the grid is refined to produce higher resolution results. This is done by testing the *convergence* of a numerical method. A numerical method is said to be convergent if the error tends to zero as the grid spacing tends to zero. That is, $e_j^n \to 0$ as $(\Delta x, \Delta t) \to (0, 0)$. Essentially,

convergence guarantees that the numerical approximation can be made arbitrarily accurate given a computer with infinite precision. Additionally, this means that smaller grid spacings provide more accurate results, and we say that any numerical error converges away.

If one wants to determine the order of convergence for a particular numerical method, one approach is to solve the PDE using three different grid spacings. In the simplest case, we assume that the grid spacings in each simulation differ by a factor of $\frac{1}{2}$. In this case, we define $\Delta x_f = \frac{1}{2}\Delta x_m = \frac{1}{2}\Delta x_c$, where the subscripts denote *fine*, *medium*, and *coarse* grid spacings, respectively. Since the functions we will be evolving are all smooth, the error of the solution will also depend smoothly on the grid spacing. In this case, we assume

$$\tilde{\phi} - \phi_{\Delta x} = C\Delta x^p + \mathcal{O}(\Delta x^{p+1}), \tag{3.18}$$

where p is the order of the numerical method, and $\phi_{\Delta x}$ represents the numerical approximation on a grid of spacing Δx. The error in a numerical solution, for smooth functions, scales with Δx^p, thus by refining the grid (reducing Δx), the error decreases, and this ratio is well-approximated by

$$\frac{\phi_{\Delta x_c} - \phi_{\Delta x_m}}{\phi_{\Delta x_m} - \phi_{\Delta x_f}} = 2^p + \mathcal{O}(\Delta x_c), \tag{3.19}$$

which can easily be shown from Eq. (3.18). By investigating this ratio, one can determine the order of convergence for a particular numerical method. We will use this approach in each of the coordinate directions to determine the temporal and spatial convergence order of the method for our method [68, 32] to evolve the correlation function.

3.2 Numerical Method for the Correlation Function

In this section, we present the method used to numerically simulate the evolution of the correlation function associated to a scalar quantum field in a given state. We present a brief description of regularizing the correlation function to remove the coincidence limit divergences; in doing so, we obtain a smooth bi-scalar function that will be used as the initial conditions in the numerical method presented. Additionally, we also demonstrate how to obtain the energy density of the field through the evolution of the correlation function. We show that the numerical methods for both the correlation function and the energy density are 2^{nd} order convergent in space and time.

3.2.1 Regularization of the Correlation Function

In analyzing the correlation functions presented in Sec. 2.3.1 it is clear to see that the vacuum correlation function (in fact, the correlation function for any state) is singular at the coincidence limit $\mathsf{x} \to \mathsf{x}'$, known as the ultraviolet divergence [5]. In general this divergence only shows up in the vacuum correlation function. The most common method is point-splitting where the energy density of a selected reference state, typically a lowest energy state, is subtracted from the energy density of the state of interest [5, 24]. This results in the expected value of the energy density being finite and produces a function that can be simulated numerically. In Minkowski spacetimes, point-splitting essentially amounts to subtracting off the vacuum correlation function from the correlation function for the state of interest. However, doing so for the vacuum state would yield an initial condition of identically zero at all grid points, resulting in a trivial solution at all times for our simulations.

As a result, if we want to numerically evolve the correlation function, a regularization must be introduced so that the correlation function is smooth and finite across the entirety of our computational domain. We consider a regularization of the vacuum correlator by replacing point-like arguments by evaluations over a thinly smeared region. This is an approach similar to that which is done in [79, 76] and is done by considering a spacetime smearing function of the form

$$F_{\mathsf{x}}(\mathsf{y}) = f_x(y) f_t(\tau), \tag{3.20}$$

where

$$f_x(y) = \frac{1}{\sqrt{2\pi\sigma_x^2}} e^{-(x-y)^2/2\sigma_x^2}, \tag{3.21}$$

$$f_t(\tau) = \frac{1}{\sqrt{2\pi\sigma_t^2}} e^{-(t-\tau)^2/2\sigma_t^2}. \tag{3.22}$$

Here σ_x is the smearing in the spatial coordinate and σ_t is the smearing in the temporal coordinate.

Notice that $F_{\mathsf{x}}(\mathsf{y})$ corresponds to a smoothed out version of the Dirac-Delta distribution centered at the spacetime point, x, and in the limit $\sigma_x \to 0$, and $\sigma_t \to 0$, we recover the original vacuum correlation function. We then define the regularized correlation function as

$$\mathcal{W}_0(\mathsf{x}, \mathsf{x}') = \int \mathrm{d}\mathsf{y}\mathrm{d}\mathsf{y}' W_0(\mathsf{y}, \mathsf{y}') F_{\mathsf{x}}(\mathsf{y}) F_{\mathsf{x}'}(\mathsf{y}'), \tag{3.23}$$

where, upon substitution of Eqs. (2.42), (3.21) and (3.22), is given by

$$\mathcal{W}_0(\mathsf{x},\mathsf{x}') = \frac{1}{\pi}\sum_{n=1}^{\infty}\frac{1}{n}e^{-k_n^2\sigma_x^2}e^{-k_n^2\sigma_t^2}\sin(k_n x)\sin(k_n x')e^{-\mathrm{i}k_n(t-t')}. \tag{3.24}$$

A full derivation of this equation is given in Appendix B. With this, we have a $C^\infty(\Omega)$ function in both spacetime arguments that can be used as an initial condition for the evolution scheme proposed in the next section.

3.2.2 Correlation Functions as Initial Boundary Value Problems

With a regularized vacuum correlation function, we provide a brief description of the necessary initial and boundary conditions that guarantee the well-posedness of the equations of motion for the correlation function. Well-posedness is a fundamental concept in the study of PDEs, ensuring that a solution to the equation not only exists and is unique but also behaves in a physically meaningful way. Additionally, well-posed problems are more likely to yield numerically stable solutions when standard computational methods are applied. We also make note of the fact that since the correlation function satisfies Eq. (2.34), the regularized correlation function $\mathcal{W}(\mathsf{x},\mathsf{x}')$ will also satisy Eq. (2.34).

We assume that our field is confined within a region $(x,x') \in [0,L]\times[0,L]$ over a temporal domain $(t,t') \in [0,T]\times[0,T]$ so that our computational domain is given by $\Omega = [0,L]^2\times[0,T]^2$. In principle, there is no need for the domains of x and x' to be the same; however, for the remainder of the thesis, we assume they are the same. Similarly, to the case of the classical scalar field, we also have to impose initial conditions and boundary conditions on the correlation function in order to fully simulate the dynamics. However, unlike the classical scalar field, we are not free to choose the initial conditions, as they are naturally imposed by initial field configuration. Moreover, we have two additional initial and boundary conditions due to the fact that the correlation function satisfies two separate PDEs.

In the case of the correlation function, we impose the following four boundary conditions that depend directly on the initial field configuration. That is, given a field state, $|\psi\rangle$, we

have the following initial conditions

$$\begin{aligned} W(\mathsf{x},\mathsf{x}')\big|_{t=t'=0} &= W^{\phi\phi}(x,x'), \\ \partial_t W(\mathsf{x},\mathsf{x}')\big|_{t=t'=0} &= W^{\pi\phi}(x,x'), \\ \partial_{t'} W(\mathsf{x},\mathsf{x}')\big|_{t=t'=0} &= W^{\phi\pi}(x,x'), \\ \partial_t\partial_{t'} W(\mathsf{x},\mathsf{x}')\big|_{t=t'=0} &= W^{\pi\pi}(x,x'). \end{aligned} \tag{3.25}$$

From Eq. (3.25), we can clearly see that the form of the initial conditions explicitly on the choice of field state, as the conjugate momentum for the field is given by $\hat{\pi}(\mathsf{x}) = \partial_t\hat{\phi}(\mathsf{x})$ and is found in the last three initial conditions.

Finally, we investigate the boundary conditions for the correlation function. As is the case for the initial conditions, the boundary conditions are also imposed by the field state directly. In our case, as was done in Sec. 3.1.1, we will that the field satisfies Dirichlet boundary conditions. Thus, our boundary conditions on the correlation function are

$$\begin{aligned} W((t,0);(t',x')) = W((t,L);(t',x')) = 0, \\ W((t,x);(t',0)) = W((t,x);(t',L)) = 0. \end{aligned} \tag{3.26}$$

With Eqs. (2.34),(3.25), and (3.26), we have a hyperbolic PDE in each of the spacetime coordinates. Given a hyperbolic PDE it is possible to show, under general conditions, the existence and uniqueness of advanced and retarded Green's functions. Given initial data for the correlation function, the correlation function can then be extended to the entire spacetime through the use of the causal propagator [34]. This extension demonstrates the well-posedness of the initial value problem for the correlation function.

3.2.3 Finite Difference Method for the Correlation Function

In Sec. 3.1.1 we demonstrated how to obtain a 2^{nd} order FD method for the $(1+1)$-dimensional scalar field in Minkowski spacetime. In this section, we will present the algorithm used to numerically evolve the correlation function of a scalar quantum field in Minkowski spacetime by utilizing many of the techniques presented in the previous section. In what follows, when we discuss the correlation function, we will be referring to the regularized correlation function in Eq. (3.24), as this is the quantity we will be simulating.

Following the procedure of Sec. 3.1.1, we first discretize our domain into a uniformly spaced grid given by the grid points $\{x_i\}_{i=0}^{N_x}$ and $\{t_n\}_{n=0}^{N_t}$. These grid points and associated grid spacings are adopted for both arguments of the correlation function so that (x,t) and

(x', t') both have the same number of grid points in the spatial and temporal components, respectively. Additionally, we define $\mathcal{W}_{ij}^{nm} \approx \mathcal{W}(x_i, t_n; x'_j, t'_m)$, where we have generalized the grid point notation to account for the second spacetime coordinate of the correlation function.

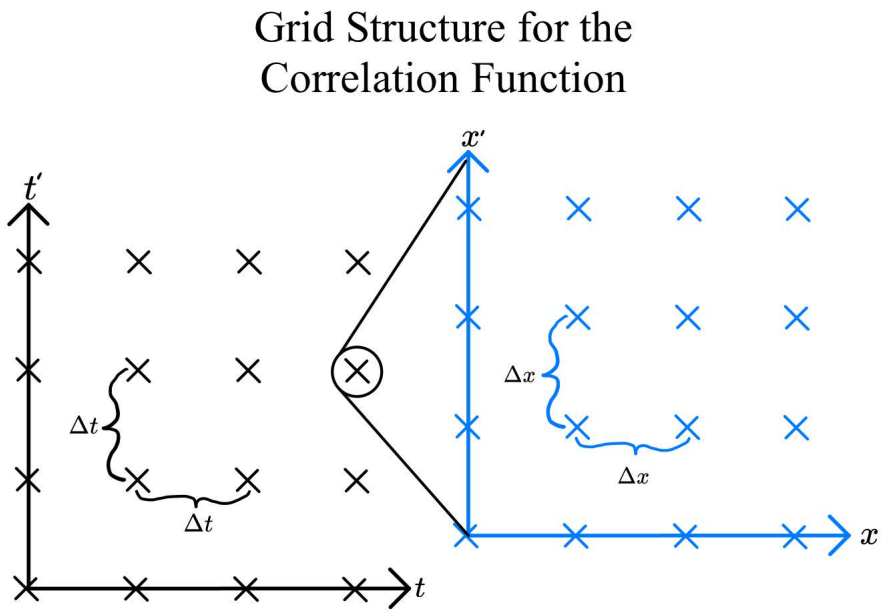

Figure 3.2: This plot demonstrates the grid structure that is used for the correlation function. The black plot represents the discretization in t and t'. We zoom in on one (t, t') grid point (blue) to show that each (t, t') grid point contains a discretization of the (x, x') coordinates.

In Fig. 3.2, we demonstrate how we can represent the discretization of the computational domain of the correlation function. This is very similar to the discretization of the wave equation, with the main difference being the addition of a second time axis in the discretization. Moreover, it is possible to see that each grid point in the (t, t')-plane contains a discretization of the (x, x')-plane. This plot also gives an intuition for how we can begin to construct the FD method for the correlation function.

In order to generalize the FD method of Sec. 3.1.1, we first note that the equations of motion for the correlation function in Eq. (2.34) act independently from one another. By utilizing this property, we first fix a particular point $(x', t') = (\tilde{x}', \tilde{t}')$ and evolve the correlation function using the FD method in the (x, t) coordinates. This results in the

following evolution equation

$$\mathcal{W}_{ij}^{(n+1)m} = 2\mathcal{W}_{ij}^{nm} - \mathcal{W}_{ij}^{(n-1)m} + C^2\left(\mathcal{W}_{(i+1)j}^{nm} - 2\mathcal{W}_{ij}^{nm} + \mathcal{W}_{(i-1)j}^{nm}\right). \tag{3.27}$$

In analyzing Eq. (3.27), we see that we now have an approximation for the correlation function along the constant t'_m-slice.

Similarly to the classical scalar field, we will run into problems with the first time steps in the t and t' direction due to the fact that we will have terms containing n (resp. m) being equal to negative one. We again fix this first time step by introducing the given initial conditions into the first time step so that we have

$$W_{ij}^{10} = W_{ij}^{00} + \Delta t W_{ij}^{\pi\phi} + \frac{1}{2}C^2\left(W_{(i+1)j}^{00} - 2W_{ij}^{00} + W_{(i-1)j}^{00}\right) \tag{3.28}$$

$$W_{ij}^{01} = W_{ij}^{00} + \Delta t W_{ij}^{\phi\pi} + \frac{1}{2}C^2\left(W_{i(j+1)}^{00} - 2W_{ij}^{00} + W_{i(j-1)}^{00}\right). \tag{3.29}$$

In doing so, we have now accounted for three out of the four prescribed initial conditions for the correlation function. To implement the fourth initial condition, we discretize both ∂_t and $\partial_{t'}$ to obtain

$$[D_t D_{t'}\mathcal{W}]_{ij}^{00} = \frac{1}{\Delta t}[D_t](\mathcal{W}_{ij}^{01} - \mathcal{W}_{ij}^{00}) = \frac{1}{\Delta t^2}(\mathcal{W}^{11} - \mathcal{W}^{01} - \mathcal{W}^{10} + \mathcal{W}^{00}) = W_{ij}^{\pi\pi}. \tag{3.30}$$

By rearranging for $\mathcal{W}_{ij}^{11}$, we get the fourth equation for our simulation that implements the initial conditions. This equation is given by

$$\mathcal{W}_{ij}^{11} = \mathcal{W}_{ij}^{01} + \mathcal{W}_{ij}^{10} - \mathcal{W}_{ij}^{00} + \Delta t^2 W_{ij}^{\pi\pi}. \tag{3.31}$$

We can then, iterate Eq. (3.27) over all values of m and j to obtain a numerical approximation to the correlation function at all values $(\mathsf{x}, \mathsf{x}') \in [0, L]^2 \times [0, T]^2$.

It is important to note that, despite the fact that we have chosen to write the evolution method by fixing $(x', t') = (\tilde{x}', \tilde{t}')$, it is in fact possible to obtain the same numerical results by instead fixing $(x, t) = (\tilde{x}, \tilde{t})$ and evolving through the (x', t') coordinates using

$$\mathcal{W}^{n(m+1)} = 2\mathcal{W}_{ij}^{nm} - \mathcal{W}_{ij}^{n(m-1)} + C^2\left(\mathcal{W}_{i(j+1)}^{nm} - 2\mathcal{W}_{ij}^{nm} + \mathcal{W}_{i(j-1)}^{nm}\right) \tag{3.32}$$

and iterating over all indices n and i.

Now that we have demonstrated how to numerically obtain the grid data for the correlation function, we move on to convergence testing and an example of how the method

can be used to generate visualizations of the correlation function.

3.2.4 Convergence Testing and Examples

We will now present the convergence test results of the numerical evolution scheme for the correlation function. Additionally, we will also give examples of the evolution of different correlation functions associated to different field configurations. It is important to note that the correlation function satisfies $W(\mathsf{x}', \mathsf{x}) = W(\mathsf{x}, \mathsf{x}')^*$. Thus, if both the real and imaginary components of the correlation function converge with order p, the symmetry allows us to conclude that we obtain the same convergence order in x' and t'.

In order to determine the convergence order of our numerical method, we will utilize the techniques discussed in Sec. 3.1.2. In particular, we numerically evolve the correlation function on three different grids, where the resolution of each grid is doubled. That is we will have a coarse, medium, and fine grid defined by the grid spacings $\Delta x_f = \frac{1}{2}\Delta x_m = \frac{1}{2}\Delta x_f$ and $\Delta t_f = \frac{1}{2}\Delta t_m = \frac{1}{2}\Delta t_c$. Then, by plotting the difference between the coarse and medium grids and the difference between the medium and fine grids, the convergence order will be determined by $\log_2$ of the multiple that makes the two plots agree.

In Fig. 3.3, we plot the real component of the difference between the coarse and medium grids along with the difference between the medium and fine grids for the numerical solution of the correlation function. We see that at each spatial grid point the two differences agree with near perfect accuracy when $h = 2$, thus we see that the real component has a spatial convergence order of 2.

In Fig. 3.4, we plot the imaginary component of the difference between the coarse and medium grids along with the difference between the medium and fine grids for the numerical solution of the correlation function. We see that at each spatial grid point the two differences agree with near perfect accuracy when $h = 2$. Thus, given Figs. 3.3 and 3.4, we can conclude that our numerical method is 2^{nd} order in space for both x and x'.

We now move on to determining the temporal convergence order of our numerical method. In order to perform the temporal convergence test, we will again compute the differences between the three grid resolutions at each time step. At each time step, we will then compute the $2-$norm of the difference and plot the $\log_2$ ratio between the norms at each time step. This will determine the temporal convergence order at each time step. Specifically,

$$p(t) = \log_2 \left(\frac{\|W^c - W^m\|_2}{\|W^m - W^f\|_2} \right) \tag{3.33}$$

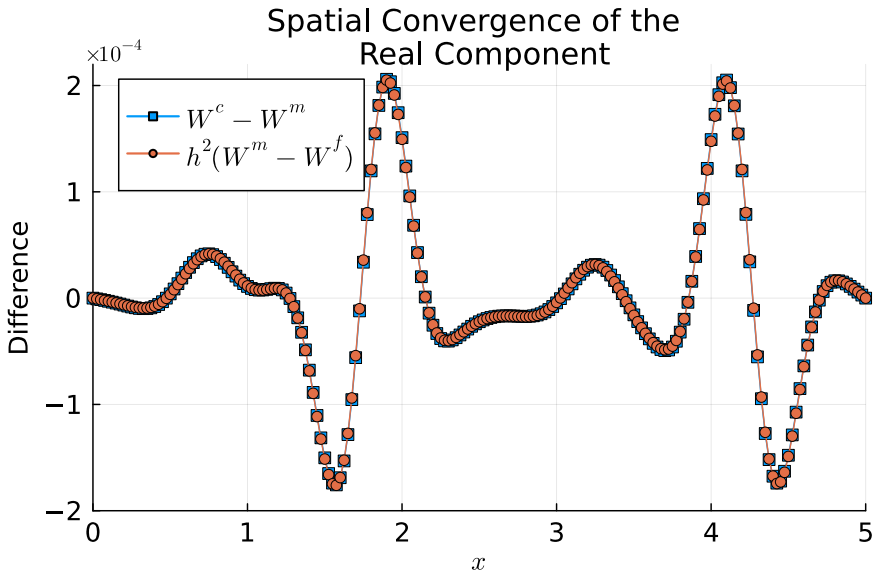

Figure 3.3: This plot is the real component difference between the coarse and medium grids and the difference between the medium and fine grids. We choose to perform the spatial convergence with $x' = 3.0$, $t' = 2.5$, and $t = 1.25$ fixed. We choose the CFL factor to be $\frac{1}{2}$, with a grid spacing of $\Delta x = 0.025$, the number of grid point is $N_x = 200$, and the resolution is halved between each grid, $h = 2$.

In Fig. 3.5, we see that the temporal convergence order is $p = 2$ for all time steps. Again, by utilizing the complex symmetry of the correlation function, we can therefore conclude that the numerical method presented for the evolution of the correlation function is 2^{nd} order in both t and t'. Thus, with Figs. 3.3, 3.4, and 3.5 we have shown that our numerical method is 2^{nd} order in both time and space.

With the results of our convergence test, we now move on to provide visualization examples of the correlation function for different field configurations. We start by first giving a visualization of the regularized vacuum correlation function given by Eq. (3.24). In Fig. 3.6 we can see how the correlation function evolves along a fixed t'-slice. Moreover, we can see similarities between the way a classical scalar field in a Dirichlet cavity would evolve. In particular, we see that, as time evolves, the maximum of the correlation function spreads away from the initial peak. Additionally, as the peaks hit the walls of our Dirichlet cavity, the values are reflected and return to their x, x' coordinates with a negative value. This is exactly what happens in the case of a 1-dimensional wave with fixed boundaries.

Recalling that the correlation function is complex-valued, we may also plot the imag-

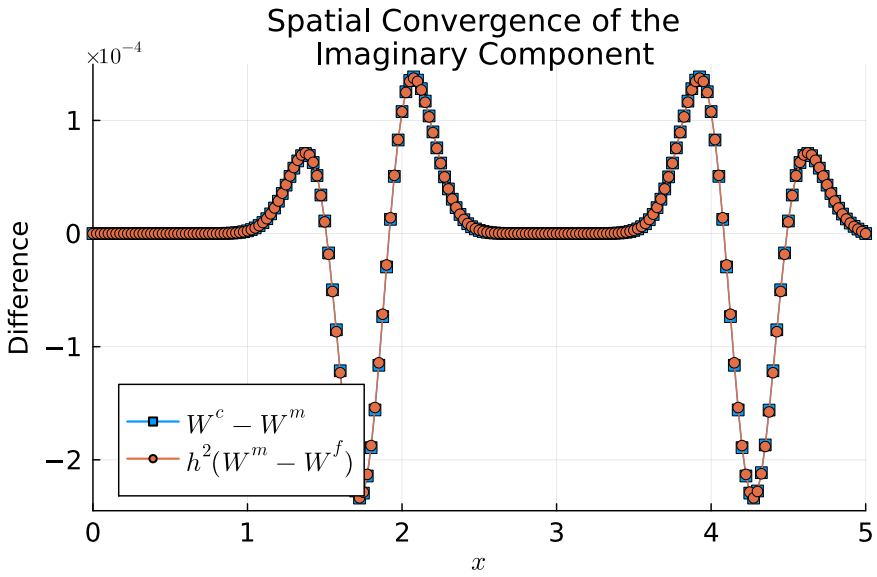

Figure 3.4: This plot is the imaginary component difference between the coarse and medium grids and the difference between the medium and fine grids. We choose to perform the spatial convergence with $x' = 3.0$, $t' = 2.5$, and $t = 1.25$ fixed. We choose the CFL factor to be $\frac{1}{2}$, with a grid spacing of $\Delta x = 0.025$, the number of grid point is $N_x = 200$, and the resolution is halved between each grid, $h = 2$.

inary component of the regularized vacuum correlation function. It is important to note that from Eq. (3.24), we can see that the imaginary component is entirely dictated by the first time derivatives in t and t'. Moreover, the imaginary component dictates the state-independent component of the correlation function. That is, for any given state, the imaginary component will evolve exactly as is shown for the vacuum correlation function.

In Fig. 3.7 we show a plot of the imaginary component at $t' = 0$ for various values of t. Similar to the case of the real component, we are able to visualize the evolution of the state independent component of the correlation function along a particular t' slice. In this case, it is also slightly easier to visualize the similarities between classical wave dynamics and the dynamics of the correlation function. In particular, we can see that the edges of the imaginary component move with exactly light speed as the boundaries follow the lines defined by $x = \pm x' - ct$ and $x = \pm x' + ct$ as is expected for the characteristic curves of the wave equation. Moreover, we can see the reflection caused by the Dirichlet boundary conditions along with the correlation function returning to the original profile after a single light crossing time of the computational domain.

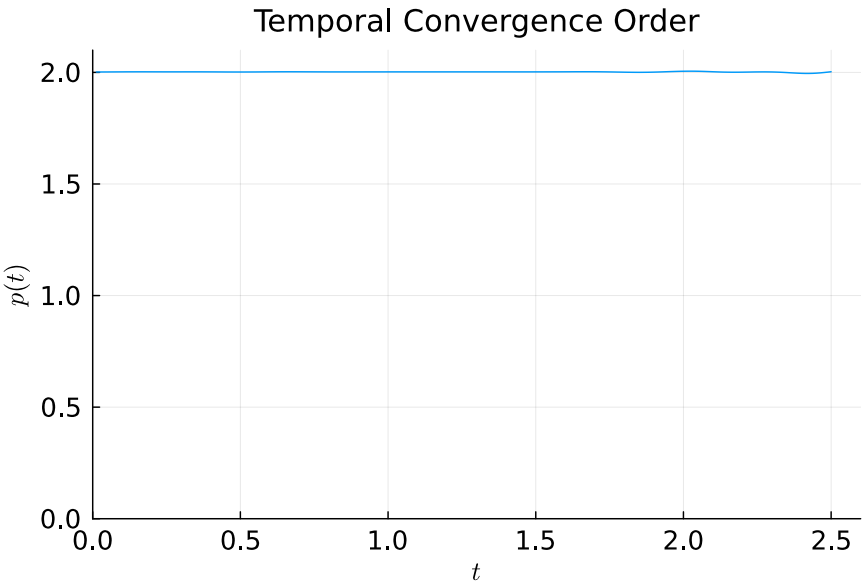

Figure 3.5: This plot is the temporal convergence order over time. The temporal spacing was chosen to be $\Delta t = 0.0125$ with $N_t = 200$. We fixed the points $x' = 3.0$, and $t' = 1.25$. As was done for the spatial convergence testing, the grid spacing is halved for each higher resolution grid.

3.3 Numerically Obtaining the Energy Density

In this Section, we will utilize the method of Sec. 3.2.3 to obtain the energy density of a particular field state. In general, one can obtain the (expectation value of the) field stress-energy tensor from the two-point correlator by evaluating

$$\langle \hat{T}_{\mu\nu} \rangle = \lim_{\mathsf{x}\to\mathsf{x}'} \left[(\partial_\mu \partial'_\nu - \frac{1}{2}\eta_{\mu\nu}\partial_\alpha \partial'^\alpha) \right] (\mathcal{W}(\mathsf{x},\mathsf{x}') - \mathcal{W}_0(\mathsf{x},\mathsf{x}')) \,, \tag{3.34}$$

where $\partial'_\nu \equiv (\partial/\partial x'^\nu)$ we are again assuming that we will be using the regularized correlation functions [11, 12]. Eq. (3.34) is known as the renormalized stress-energy tensor, and by subtracting off the vacuum correlation function, we can remove the divergence seen in Eq. (2.35).

Of particular importance in this section and the remainder of this work, is the energy density, or the $\langle \hat{T}_{00} \rangle$ component of the stress energy tensor. By evaluating this component,

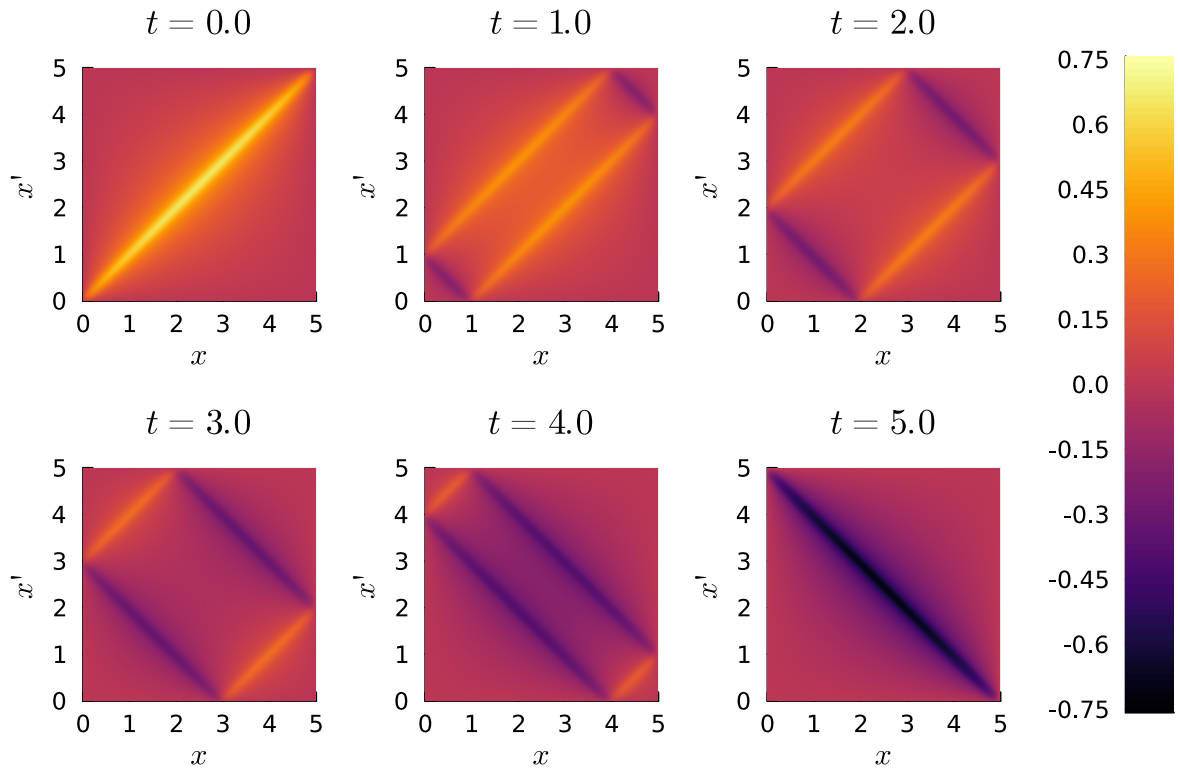

Figure 3.6: A plot of the real component of the regularized vacuum correlation function at $t' = 0$ for various values of t.

we find that

$$\langle \hat{T}_{00} \rangle = \frac{1}{2} \lim_{\mathsf{x} \to \mathsf{x}'} \left[\partial_x \partial_{x'} + \partial_t \partial_{t'} \right] \mathcal{W}_{\mathrm{R}}(\mathsf{x}, \mathsf{x}'), \tag{3.35}$$

where $\mathcal{W}_{\mathrm{R}}(\mathsf{x}, \mathsf{x}') = \mathcal{W}(\mathsf{x}, \mathsf{x}') - \mathcal{W}_0(\mathsf{x}, \mathsf{x}')$ is the regularized, renormalized correlation function. We again discretize the derivatives, and obtain the following

$$\langle \hat{T}_{00} \rangle = \frac{1}{2} \left([D_t D_{t'} \mathcal{W}_{\mathrm{R}}]_{ij}^{nm} + [D_x D_{x'} \mathcal{W}_{\mathrm{R}}]_{ij}^{nm} \right) \Big|_{n=m, i=j}. \tag{3.36}$$

Notice that we can compute the limit exactly by evaluating the numerical approximation at $n = m$ and $i = j$ since we have discretized the domain into equal grid spacings for each of the temporal and spatial directions. For each of the discretized derivatives in Eq. (3.36)

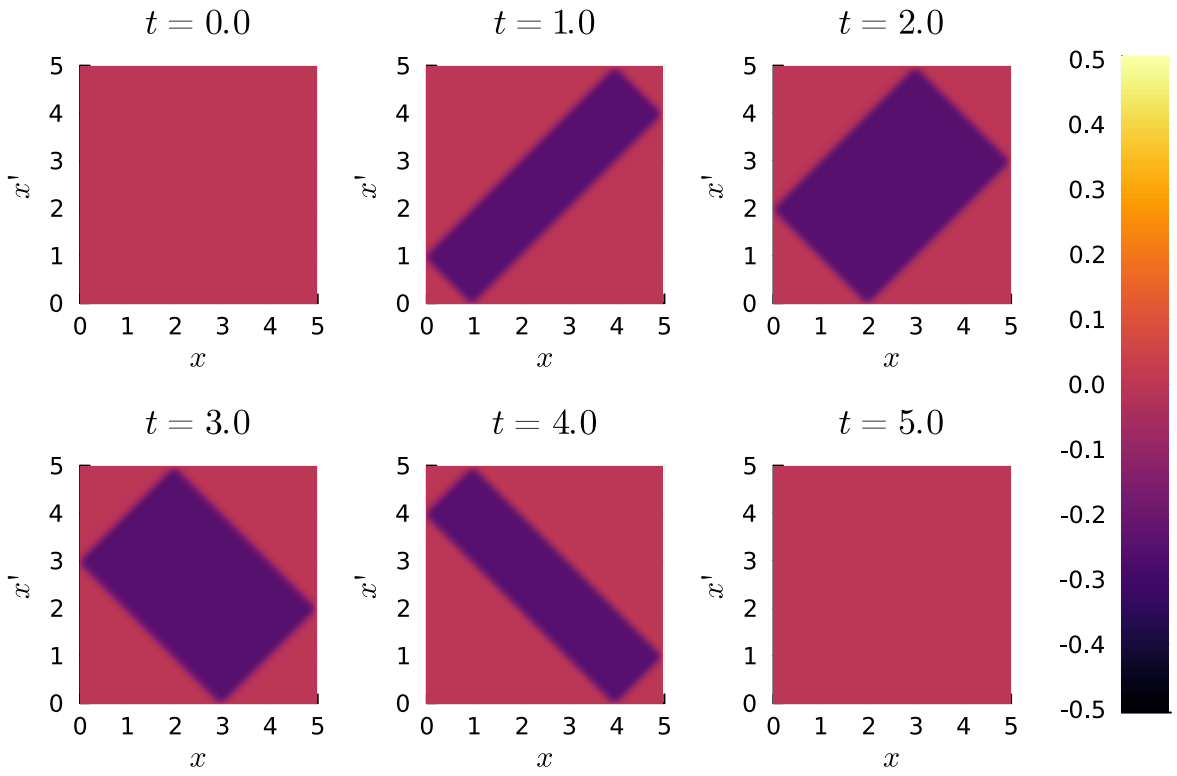

Figure 3.7: A plot of the imaginary component of the regularized vacuum correlation function at $t' = 0$ for various values of t.

we have explicit expressions given by

$$[D_t D_{t'} \mathcal{W}]^{nn}_{ii} = \frac{1}{4\Delta t^2} \left(\mathcal{W}^{(n+1)(n+1)}_{ii} - \mathcal{W}^{(n-1)(n+1)}_{ii} - \mathcal{W}^{(n+1)(n-1)}_{ii} + \mathcal{W}^{(n-1)(n-1)}_{ii} \right), \quad (3.37)$$

$$[D_x D_{x'} \mathcal{W}]^{nn}_{ii} = \frac{1}{4\Delta x^2} \left(\mathcal{W}^{nn}_{(i+1)(i+1)} - \mathcal{W}^{nn}_{(i-1)(i+1)} - \mathcal{W}^{nn}_{(i+1)(i-1)} + \mathcal{W}^{nn}_{(i-1)(i-1)} \right). \quad (3.38)$$

As was the case in evolving the correlation function, there are special cases that must be taken into account when numerically evaluating the energy density. We first demonstrate the special cases in the time derivatives. In the case where $n = 1$, we notice that we will have terms of the form $\mathcal{W}^{0-1}_{ii}$, $\mathcal{W}^{-10}_{ii}$, and $\mathcal{W}^{-1-1}_{ii}$. However, unlike the evolution of the correlation function, we do not have additional parameters such as initial conditions that can be used to remove these terms. Instead, we use a 1^{st} order discrete derivative of the

form

$$[D_t f]_i^n = \frac{1}{\Delta t}\left(f_i^{n+1} - f_i^n\right), \tag{3.39}$$

which yields the following result when $n = 0$

$$[D_t D_{t'} \mathcal{W}]_{ii}^{00} = \frac{1}{\Delta t^2}\left(\mathcal{W}_{ii}^{11} - \mathcal{W}_{ii}^{10} - \mathcal{W}_{ii}^{01} + \mathcal{W}_{ii}^{00}\right). \tag{3.40}$$

Similarly, for the spatial derivatives, we will have indices that have values of negative one, and we will use a 1^{st} order spatial derivative of the form

$$[D_x f]_0^n = \frac{1}{\Delta x}\left(f_1^n - f_0^n\right), \tag{3.41}$$

$$[D_x f]_{\text{end}}^n = \frac{1}{\Delta x}\left(f_{\text{end}}^n - f_{\text{end}-1}^n\right). \tag{3.42}$$

This yields two separate equations that account for cases where $i \in \{0, Nx\}$. These expressions are given by

$$[D_x D_{x'} \mathcal{W}]_{00}^{nn} = \frac{1}{\Delta x^2}\left(\mathcal{W}_{11}^{nn} - \mathcal{W}_{10}^{nn} - \mathcal{W}_{01}^{nn} + \mathcal{W}_{00}^{nn}\right), \tag{3.43}$$

$$[D_x D_{x'} \mathcal{W}]_{\text{end,end}}^{nn} = \frac{1}{\Delta x^2}\left(\mathcal{W}_{\text{end,end}}^{nn} - \mathcal{W}_{\text{end(end}-1)}^{nn} - \mathcal{W}_{(\text{end}-1)\text{end}}^{nn} + \mathcal{W}_{(\text{end}-1)(\text{end}-1)}^{nn}\right). \tag{3.44}$$

By utilizing Eqs. (3.37) and (3.38), along with the special cases of Eqs. (3.40), (3.43), and (3.44), we can evaluate the energy density at each time step to provide simulations of how the energy density evolves over time. This is useful, not only for understanding the dynamics of our quantum field, but can also be used to study the energy of our system as a function of time. Since we have grid data at each spatial and temporal time step, we can use a numerical integration method to integrate the energy density over the spatial domain to obtain the total energy at a given time. In particular, we employ a trapezoidal rule to numerically integrate the spatial domain. As this is also a 2^{nd} order method, it will maintain the accuracy of all other methods that have been used thus far. This will be used when we want to verify that our numerical method is not dissipating energy (in the case of quantum field confined to a cavity with no external potential) and in later sections when studying the effectiveness of a confining potential well.

3.3.1 Convergence Testing and Examples

As was done for the correlation function in Sec. 3.2.4, we must ensure that our numerical method is convergent and to what order. We will follow the same approach taken previously where we utilize three grids of different grid spacings where each higher resolution has double the number of grid points. That is, $\Delta x_f = \frac{1}{2}\Delta x_m = \frac{1}{4}\Delta x_c$ and $\Delta t_f = \frac{1}{2}\Delta t_m = \frac{1}{4}\Delta t_c$. Unlike the case for the correlation function, the energy density is a purely real quantity and thus we will only need to check the spatial and temporal convergence order in the real components. We will again determine the spatial convergence order by plotting the difference between the coarse and medium grids and the difference between the medium and fine grids to find the factor that makes the plots agree.

In order to study the convergence, we will analyze the evolution of a one-particle state given by

$$|\psi\rangle = \frac{1}{\lambda}\sum_{n=1}^{N} e^{-\alpha^2 k_n^2/2} e^{\mathrm{i}k_n x_0} |n\rangle \,, \tag{3.45}$$

where x_0 is where the wavepacket is centered, $k_n = \frac{n\pi}{L}$, and α is a parameter that controls the width of the wavepacket. In Fig. 3.8 we plot an example of the initial wavepacket for different values of α to demonstrate how one can control the desired shape of the energy distribution.

We will also only use the state dependent component of the correlation functions, since this implies that we have already renormalized the energy density by subtracting off the vacuum correlation function as demonstrated in Eq. (3.35). In Fig. 3.9 we plot the difference between the coarse and medium resolution grids along with the medium and fine grids to determine the spatial convergence order of the numerical method used to solve for the energy density.

In general, one would expect that the numerical method prescribed in Sec. 3.3 should be 2^{nd} order as we are using a second order FD scheme for the derivatives in both time and space. We see in Fig. 3.9 that the the grid points agree when the power of h is chosen to be 2, thus our method is 2^{nd} order in space.

Given that our method is 2^{nd} order in space, we can move on to utilizing Eq. (3.33) to determine the temporal convergence order of our numerical method. We can see in Fig. 3.10 that our method is 2^{nd} order convergent in time throughout the duration of the simulation. We notice that at $t = 5$ the convergence order deviates slightly. This is due to the fact that, at the boundaries we are utilizing Eqs. (3.43) and (3.44) which are both 1^{st} order to compensate for the lack of a grid point to the left (resp. right) of the $x = 0$ (resp. $x = L$) boundary. Given the results of Figs. 3.9 and 3.10 we can conclude that our method

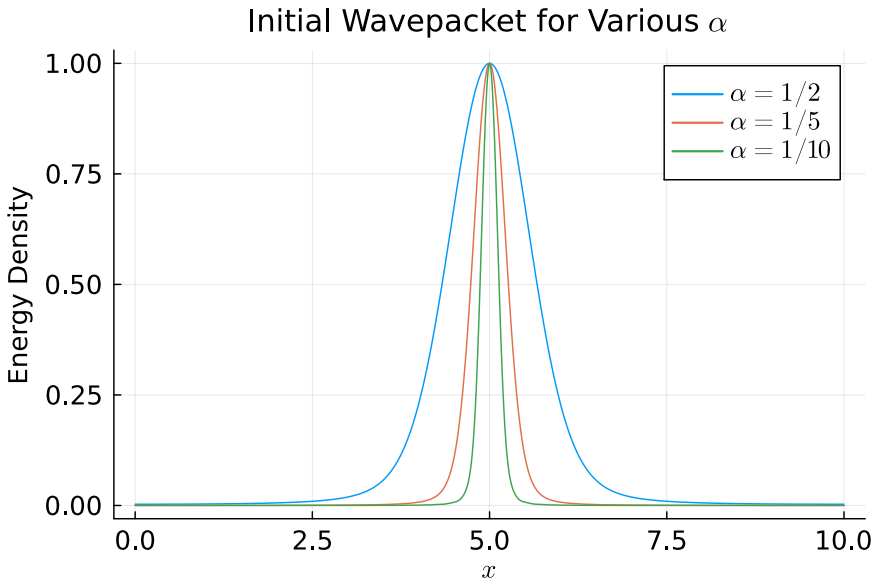

Figure 3.8: This plot shows the initial wavepacket for various values of α. In order to create the wavepacket, we used $N = 100$ modes and selected $x_0 = 5$. Additionally, we scaled each of the curves so that it was possible to see how the width changes with α.

for numerically evaluating the energy density of our field is 2^{nd} order in both space and time.

Given that our method is 2^{nd} order in both time and space, we can move on to providing an example of the energy density as a function of time. By utilizing, Eq. (3.45) we can use Eq. (2.45) to find the appropriate initial conditions for the correlation function in order to solve for the energy density. In Fig. 3.11, we plot the energy density at various times to get a visualization of the energy density. We can see that at $t = 0.0$ we have a wavepacket that has a Gaussian shape as is expected from the field configuration of Eq. (3.45). As the evolution progress, we see that the energy density splits into left and right moving wavepackets that are each half the value of the original wavepacket, but maintain the shape of the original wavepacket. This is exactly what one would expect when analyzing Eq. (3.35), which is precisely the $(1+1)$-dimensional wave equation in the limit $\mathsf{x} \to \mathsf{x}'$. Moreover, we can see that by imposing Dirichlet boundary conditions on the correlation function, we obtain solutions for the energy density that act as though the walls are perfectly reflecting. That is, the energy density has Neumann boundary conditions.

Given that we have no external forces in our equation of motion and the energy density satisfies Neumann boundary conditions, one expects that the energy over time is constant.

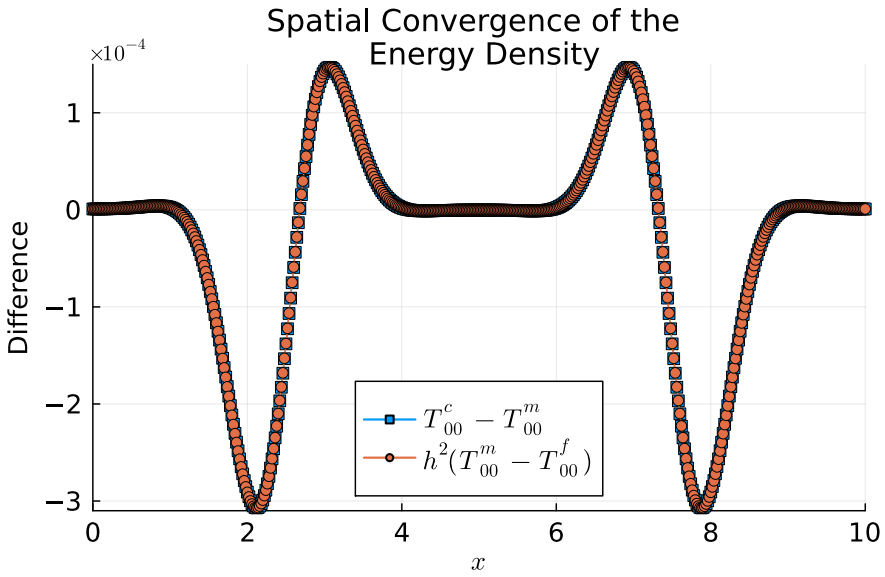

Figure 3.9: This plot is for the difference between the coarse and medium grids and the difference between the medium and fine grids for the energy density. We chose to evaluate this spatial convergence at $t = 2.5$, a CFL factor of $\frac{1}{2}$, a grid spacing of $\Delta x = 0.02$ and $N_x = 500$ grid points. For each resolution the grid spacing is halved so that $h = 2$.

In Fig. 3.12 we perform a final check of our numerical method by plotting the total energy at each time step by integrating the energy density over the computational domain. For our numerical integration method, we will use a trapezoidal rule which is known to be 2^{nd} order convergent [45]. The trapezoid rule for numerical integration for a 1-dimensional function $f(x)$ is defined as

$$\int_a^b \mathrm{d}x f(x) = \frac{\Delta x}{2}(f_0 + f_N) + \Delta x \sum_{i=1}^{N-1} f_i, \tag{3.46}$$

where Δx is the grid spacing, and N is the number of grid points that are used in the simulation. We can see in Fig. 3.12 that the total energy of our field remains constant over time. This is exactly what is expected and demonstrates that, on the time scales we are working on, that our numerical method is not dissipating energy. In fact, it can be shown that the particular method we are using should not dissipate energy even in long time simulations [75, 16]. Thus, we have demonstrated an effective and convergent numerical method for evaluating the energy density of a given field configuration through

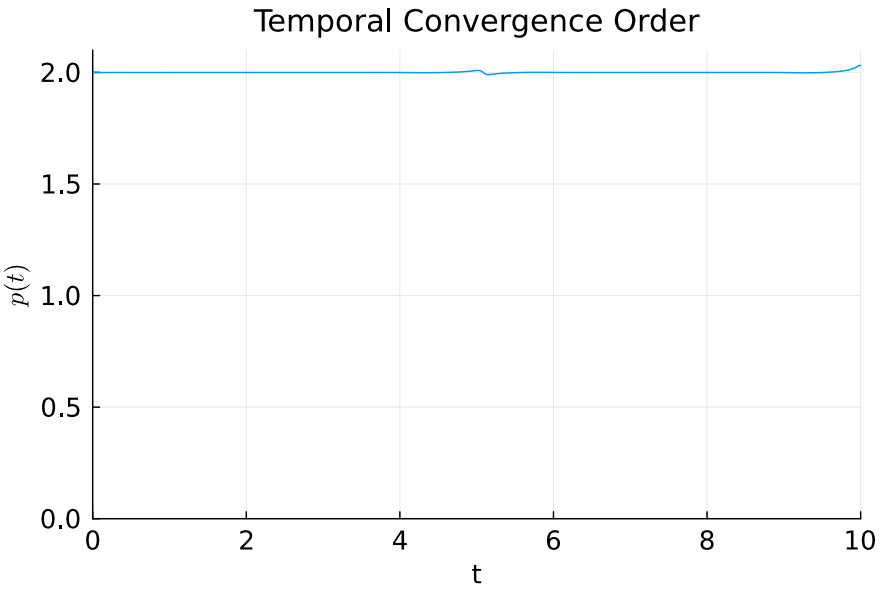

Figure 3.10: This plot is the temporal convergence order over time for the energy density. We chose a CFL factor of $\frac{1}{2}$, a grid spacing of $\Delta t = 0.01$ and $N_x = 1000$ grid points. For each resolution the grid spacing is halved.

the evolution of the correlation function. We now move on to how we optimized this particular numerical method in order to run longer time simulations.

3.4 Optimization of the Time Evolution

The final aspect of our numerical method that must be discussed is optimization. Optimization is an important part of designing algorithms that can be used for analyzing many different scenarios. In our case, there are two primary ways in which we optimize our algorithm, speed and memory.

In terms of optimizing speed, we took the approach of using *parallelization* for the discrete spatial derivatives. We utilize the `@batch` macro from `Polyseter.jl` package to implement the parallelization across each of the threads. To accomplish this, each function is passed two separate arrays that we label as `read` and `write`. The `read` array has the stored data from the previous two time steps, while the `write` array is empty and will only store the output of the current evaluation. By doing so, each thread in the parallelization has access to the array denoted `read`, and then performs the spatial derivatives of Eq. (3.27)

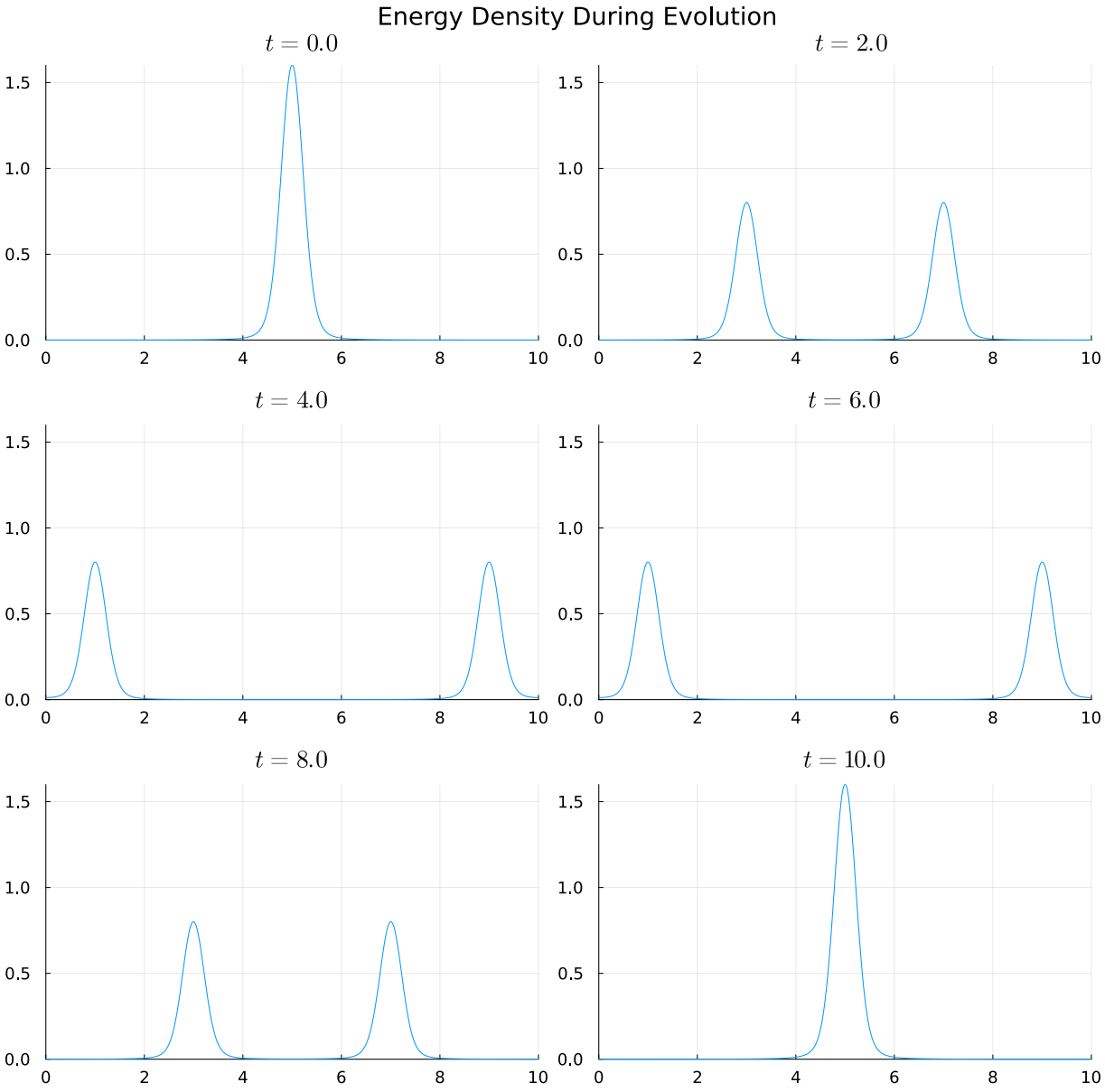

Figure 3.11: This is a plot of the energy density at different times throughout the evolution. We have created our wavepacket using $x_0 = 5$, $\alpha = \frac{1}{5}$, and $N = 100$. We use $N_x = 1000$ grid points and a CFL factor of $\frac{1}{2}$ for the evolution.

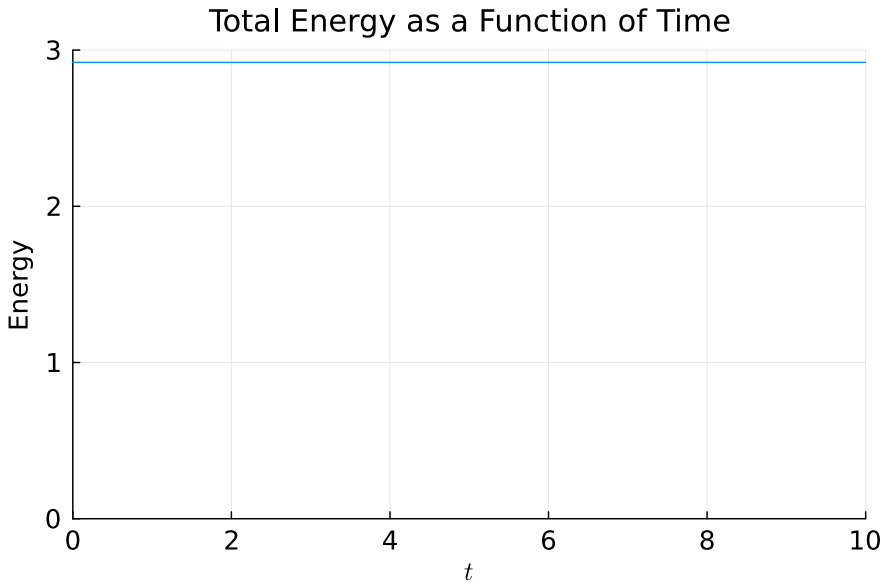

Figure 3.12: This is a plot of the total energy of our field as a function of time. For our wavepacket we choose $\alpha = 1/5$, $N = 100$ modes, and $x_0 = 5.0$.

in parallel. That is, we simultaneously calculate the derivatives at the i^{th} index, and the number of parallel calculations depends on the number of threads that are available on a given device. Following the evaluation of the discrete derivatives, the values are then stored into the `write` array.

By only parallelizing the spatial derivatives, this avoids what are known as *race conditions*, in which one thread is performing an evaluation without the necessary data. An example of how this can occur can be seen if we consider a scenario in which thread 2 is asked to compute the $n = 4$ time step, and thread 1 is asked to compute the $n = 3$ time step. If thread 2 begins its process before thread 1 has finished, then thread 2 will be evaluating Eq. (3.27) without the data from the $n = 3$ time step resulting in incorrect solutions. Additionally, by defining a `read` and `write` array, we will never be writing necessary data to the same array that is being used for current calculations. This prevents any possible overwriting of necessary values, or incorrect evaluations. Once all spatial derivatives are calculated at a particular time step, we update the `read` array with the values that have been stored in the `write` array, and continue on to the next time step.

The second way that we optimized our algorithm is by decreasing the necessary memory required to perform certain evaluations. In general, a finite difference method requires $\mathcal{O}(N^d)$ memory to store all data points. In this case, N is the number of grid points in a

particular coordinate direction, and d is the dimensionality of the problem, in this case, $d = 4$. This creates a competition between how well one wants to spatially resolve a simulation, and how long (how many time steps) the simulation can be performed on a particular machine. In the case that one only needs the correlation function at particular instances in time, for example in the case of the energy density which only requires equal time values of the correlation function, we can drastically decrease the memory requirements.

In particular, we can decrease the memory requirements through two important methods. The first is recognizing that the wave equation only depends on data from two previous time steps to evaluate the next time step. The second, is that, for everything we study in this thesis, we will only need data about the correlation function along the equal time slices. Instead of allocating an array for every time-step and spatial grid point, we can instead allocate a four-dimensional array that is $N_x \times N_x \times 3 \times 3$. This allows us to evolve only a necessary "slab" of data, from which we can then overwrite the slab data by simply overwriting the previous data with the new data and proceeding forward in this manner. In doing so, we can compute the energy density at a given time step, evolve the slab forward in t and then forward in t' and again evaluate the energy density. By proceeding forward in this fashion, if we have the memory to allocate the array holding this slab, we can, in theory, evolve simulations for as long as we want. We call this evolution a *diagonal evolution* as we are only evolving along the $t = t'$ diagonal to achieve the numerical results necessary for our particular simulations. In addition to improving the memory necessary for our evolution, this method also yields a notable speed improvement for our simulations as we no longer need to evolve over the entire domain, but instead only need a particular subset of time-steps. Scripts and examples of this code can be found on GitHub at [56]

In Fig. 3.13, we show how we evolve the slab along the equal time slice $t = t'$. Specifically, we show, given grid data from the `slab_read` array, how one can use Eq. (3.32) to first evolve the slab forward in t' by one time step. The data is stored in `slab_write` and `slab_read` is then overwritten with the data of `slab_write` yielding the dashed blue square. The dashed blue square is now our new slab, which is evolved forward in t one time step using Eq. (3.27). We follow the same procedure of writing to `slab_write` and overwriting the data of `slab_read` to yield the purple square, which is now a slab of data centered on the $t = t'$ slice. With Fig. 3.13, it is clear why this method is significantly more efficient in terms of both speed and memory when comparing to an evolution across all points in the domain.

Additionally, this method can be modified for evolution of the correlation function in cases where data at only a specific t, t' coordinate is necessary. For example, if we only need the data for the correlation function at the point $(t, t') = (T_1, T_2)$, we could simply evolve the slab "up" to T_2 and then evolve the slab "right" to T_1. In general, with few

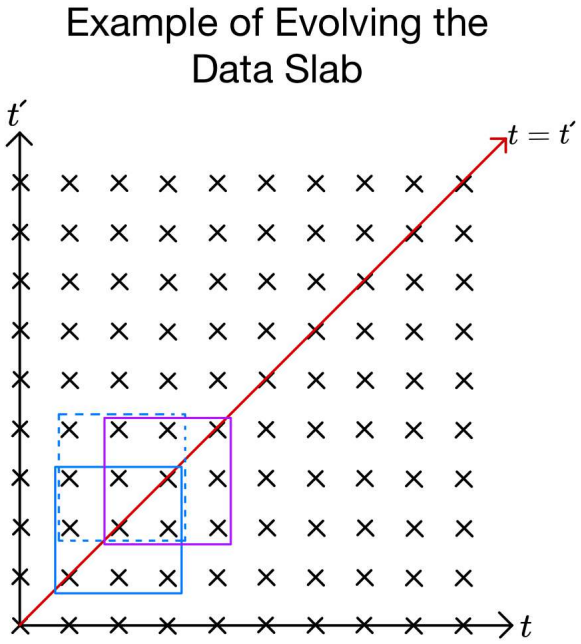

Figure 3.13: This demonstrates how to visualize the diagonal evolution of the slab. The solid blue square represents the current data stored to the `slab_read` array. The slab is evolved "up", represented by the dashed blue square, and then evolved "right", the purple square.

modifications, this method could also be adapted to have the slab "scan" across all points in the computational domain and perform necessary calculations with the slab data in scenarios where data in the whole domain is necessary, (e.g. entanglement harvesting calculations where the correlation function is integrated over the whole spacetime). In what follows, we will utilize the diagonal evolution to evolve the correlation function in the presence of a time-dependent confining potential well.

Chapter 4

Dynamic Localization

In this chapter, we will utilize the methods of Sec. 3.2.3 to dynamically localize a massless scalar quantum field. We study the effects of a time-dependent confining potential well on both the energy density and purity of the localized degrees of freedom of the quantum field.

4.1 Localized Quantum Fields

The formalism for understanding localized quantum fields is similar to that of the quantum scalar field presented in Sec 2. We adapt Eq. 2.1 with the addition of some external time-dependent potential well as follows

$$S = -\frac{1}{2}\int \mathrm{d}^d x \left(\eta^{\mu\nu}\partial_\mu\phi\,\partial_\nu\phi + V(\mathsf{x})\phi^2\right), \tag{4.1}$$

which yields the equation of motion

$$[\partial_\mu\partial^\mu - V(\mathsf{x})]\phi(\mathsf{x}) = 0. \tag{4.2}$$

As was done in Sec. 2, we can write the general solution to Eq.(4.2) as

$$\phi(\mathsf{x}) = \sum_j \left(a_j u_j(\mathsf{x}) + a_j^* u_j^*(\mathsf{x})\right), \tag{4.3}$$

where $\{u_j(\mathsf{x})\}$ is again a complex basis of solutions to Eq. (4.2), that, in the event that the confining potential is time-dependent, will not be the same as those in Eq (2.12).

Given Eq. (4.3), we can follow the canonical quantization procedure described in Sec. 2 to quantize the classical field, upgrading it to a quantum field. Interestingly, if we set $V(\mathsf{x}) = m^2$ for a constant $m \geq 0$, then this procedure is nothing more than the theory of a Klein-Gordon field of mass m in flat spacetime. In this case, we can choose the complete set of basis functions to be the planes waves discussed previously. It is also important to note that, for our numerical simulations, the CFL factor presented in Sec. 3.1.2 must be adapted to account for the inclusion of the external potential term. In this case, the CFL factor must be chosen such that the following condition (see Appendix C) is met

$$\Delta t^2 \leq \frac{\Delta x^2}{1 + \frac{1}{2}\tilde{V}}, \tag{4.4}$$

where $\tilde{V}$ is the maximum value attained by the potential.

It is also possible to consider cases where $V(\mathsf{x})$ has a nontrivial spacetime dependence. As a result, this will impact the shape of the set of mode functions $\{u_j(\mathsf{x})\}$ used as the basis of solutions for Eq. (4.3), as well as determining if the labels are discrete or continuous. If the potential is static - i.e., if $V(\mathsf{x}) = V(\boldsymbol{x})$ is independent of the inertial time coordinate in a given inertial frame - one can find a basis of solutions which separates as $e^{-\mathrm{i}\omega_j t} f_j(\boldsymbol{x})$. In general, however, the lack of translational invariance means that the spatial profile, $f_j(\boldsymbol{x})$, will not be given by pure plane waves.

A case of particular interest is that of an external potential $V(\boldsymbol{x})$ that grows to infinity as the distance between $\boldsymbol{x}$ and some finite region of space increases, such that all of the spatial profiles $f_j(\boldsymbol{x})$ will be strongly localized in a region around the minima of the potential. In this scenario, we say that $\hat{\phi}(\mathsf{x})$ is a *localized quantum field*: every admissible field configuration will effectively be confined in a localized region of space determined by the region of strong support of the basis functions $f_j(\boldsymbol{x})$. Localized quantum field theories of this type are particularly relevant to the construction of fully relativistic versions of particle detector models [21, 18, 49, 71]. However, there is discussion about the reality of using external potentials that tend to infinity, as well as how effective these fields are when used as particle detectors. One of the main problems raised in using these localized fields as particle detectors is that, when physically localizing these fields, the external potential must be time-dependent. As a result, it is believed that the injection of energy from creating the external potential into the field will result in a field configuration that is too mixed to effectively detect particles.

The goal in the rest of this chapter will be to study the price one pays when dynamically constructing localized quantum field theories from a free field theory, both from the energetic and entropic point of view. We do this by starting with a free Klein-Gordon field and then applying a time-dependent external potential $V(\mathsf{x})$ which grows for a finite period of time, until it stabilizes in a shape that mimics a confining cavity, modeling the construction of a realistically confined field.

As was mentioned in Sec. 2.2 and seen in Sec. 3.2, our methods rely on calculations in a finite computational domain. In this case, the cavity two-point function becomes the starting point for the field theory in free space, within the limits of our computational domain. In other words, what we call free space will be a large enough cavity, within which we will grow a smaller potential in a smaller region representing the realistic cavity.

4.2 Energy Density Behaviour in Dynamical Cavity Creation

The confining potential that will be used in our study is chosen in such a way that the spatial profile is a smooth approximation to a square cavity. As for the time dependence of the potential, we choose it to grow linearly in time, up to some predetermined time $T_{\max}$. The specific potential is thus given by

$$V(x,t) = V_{\max}\frac{t}{T_{\max}}\Big(e^{-(x-x_{\mathrm{L}})^2/\ell^2}[1+\mathrm{erf}(-\beta(x-x_{\mathrm{L}}))] + e^{-(x-x_{\mathrm{R}})^2/\ell^2}[1+\mathrm{erf}(\beta(x-x_{\mathrm{R}}))]\Big). \tag{4.5}$$

In this equation, $\mathrm{erf}(x)$ is the error function, $V_{\max}$ is a prefactor chosen to control the height of the potential after it stops growing, β determines how sharp the interior walls of the cavity are, and ℓ determines the width of the potential walls. x_{L} and x_{R} are the location of the maxima of the left and right walls, respectively.

In Fig. 4.1, we show the potential after the cutoff time, $t > T_{\max}$ with various values of β. From this figure, it is clear how, for large values of β, this confining potential mimics that of a rectangular well. The efficacy of this potential will be explored in more detail in the next section.

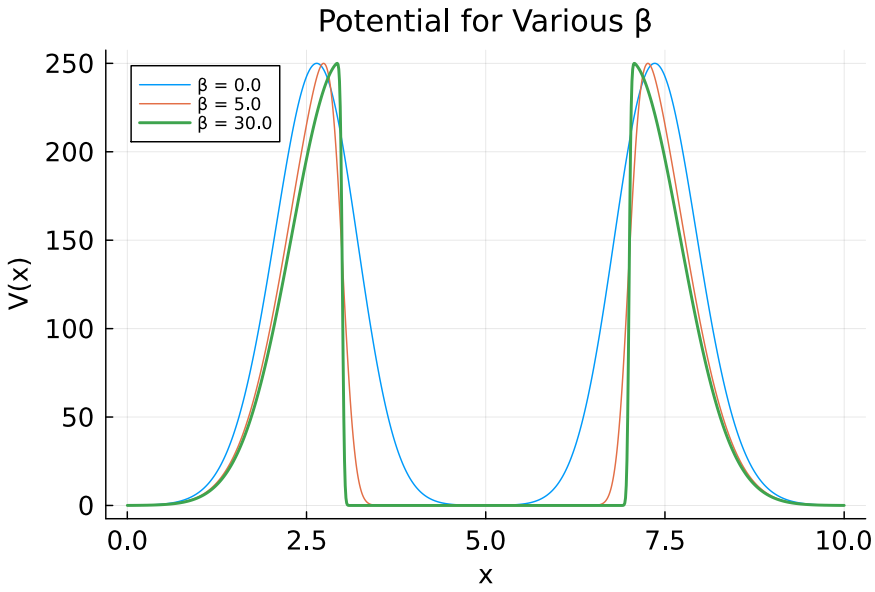

Figure 4.1: This plot shows the choice of confining potential for different choices of β when $t \geq T_{\max}$, with $V_{\max} = 250$, $x_{\mathrm{L}} = 3$, and $x_{\mathrm{R}} = 7$.

4.2.1 Confining Power of the Effective Cavity

Before doing a full dynamic simulation for the growth of the potential, it is instructive to test the extent to which the potential at late times (once the walls of the cavity are fully raised) is capable of confining field excitations. This is done by considering a static potential given by Eq. (4.5) at $t = T_{\max}$ is at confining a localized wavepacket. We first define a state whose energy is localized within the interior region of the cavity. The particular localization that we chose is

$$|\psi\rangle = \frac{1}{\lambda} \sum_{n=1}^{N} e^{-\alpha^2 k_n^2/2} e^{\mathrm{i}k_n x_0} |n\rangle \,, \tag{4.6}$$

where λ is a normalization constant for the state, α is a parameter that controls the width of the wavepacket, x_0 is the spatial location for the peak of the wavepacket, and N is the number of modes we choose to create our wavepacket. The initial energy distribution of the field given this equation can be visualized in Fig. 3.8.

When comparing Fig. 4.2 to Fig. 4.1, we see that the field state is localized at the center of the confining potential with the peak located at $l = 2.5$ away from the edges.

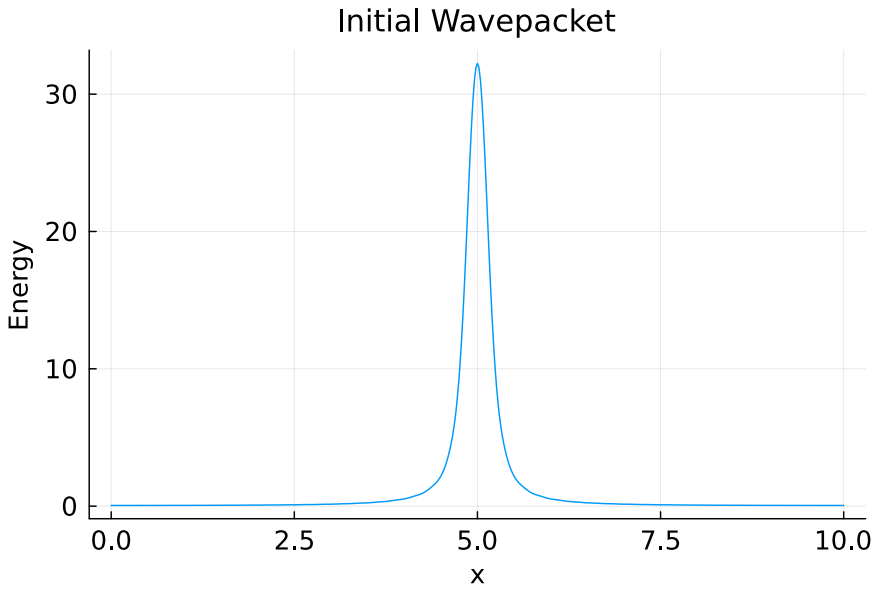

Figure 4.2: Initial Energy distribution of the localized wavepacket, where $N = 100$ modes were used with $\alpha = 1/11$, and $x_0 = 5.0$.

Then, we can plot the energy of the interior and exterior regions of the cavity as a function of time to determine how effective our cavity is at preventing transmission through the walls.

In Fig. 4.3 we see that the cavity is not perfectly confining as is the case for an infinite wall, which is expected since this potential is finite. In Fig. 4.3, the left wall of the cavity is chosen to $x_{\text{left}} = 2.4$ and the right wall of the cavity is chosen to be $x_{\text{right}} = 7.6$. In comparing with Fig. 4.1, we determined these values to be reasonably aligned with the outer boundaries of the potential.

At approximately $t = 2.75$, we see that some energy is able to penetrate the walls of the cavity. However, for the choice of parameters $\beta = 30$ and $\ell = 1$ very little energy actually leaves the cavity as exemplified by the overall small increase in energy in the exterior region. This is even better illustrated by looking at the quality factor Q of the potential wall seen as a confining cavity. This is defined as

$$Q = \frac{(\text{initial energy stored inside at } t = 0)}{(\text{energy lost in a cycle})}, \tag{4.7}$$

where, for a massless field in our setup, "one cycle" of the system corresponds to one light-

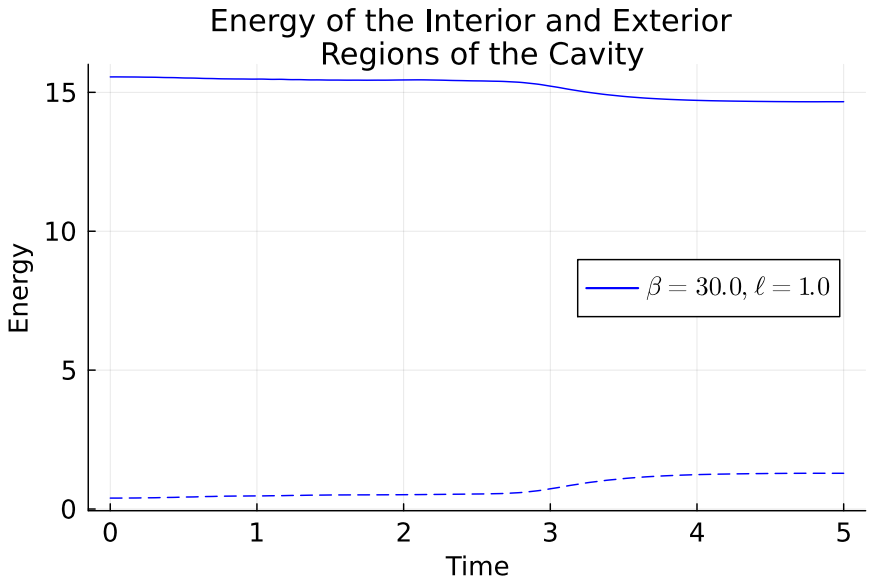

Figure 4.3: Energy as a function of time in the interior of the cavity and on the exterior of the cavity for $\ell = 1.0$, and $\beta = 30.0$. The cavity is chosen so that $x_{\text{left}} = 2.4$ and $x_{\text{right}} = 7.6$. The solid line represents the energy in the interior of the cavity, while the dashed line is the energy in the exterior region of the cavity.

crossing time of the effective cavity whose walls are described by the external potential. In the case of our analysis, one-light crossing time is with respect to the cavity defined by $x_{\text{left}} = 2.4$ and $x_{\text{right}} = 7.6$ as discussed previously. For a one-particle state of the form

$$|\psi\rangle = \sum_n c_n |n\rangle \,, \tag{4.8}$$

we can express the quality factor as

$$Q = \frac{\sum_n |c_n|^2 \omega_n}{\sum_n |T(\omega_n) c_n|^2 \omega_n}, \tag{4.9}$$

where $T(\omega_n)$ is the transmissivity of the potential for a mode with frequency ω_n that emanates from inside of the cavity.

For a general potential, the transmissivity can only be computed numerically - and in fact, this will be investigated. However, to build an intuition for what is expected with our potential, it is useful to approximate the potential walls by top-hat functions with a

given height V_0 and width a. These should, roughly, correspond to the parameters $V_{\max}$ and ℓ, respectively. For top-hat potential barriers, the transmissivity coefficients can be computed exactly, and are given by

$$|T(\omega)|^2 = \begin{cases} \dfrac{4\kappa^2\omega^2}{4\kappa^2\omega^2 + V_0^2\sinh^2(\kappa a)}, & \omega^2 - V_0 < 0, \\ \dfrac{4K^2\omega^2}{4K^2\omega^2 + V_0^2\sin^2(Ka)}, & \omega^2 - V_0 \geq 0 \end{cases} \tag{4.10}$$

where in the first case in Eq. (4.10) we define $\kappa \equiv \sqrt{V_0 - \omega^2}$, and in the second case we define $K = \sqrt{\omega^2 - V_0}$. Thus, for an initial wavepacket of the form in Eq. (4.6), we can estimate the quality factor of the effective cavity by

$$Q = \frac{\sum_{n=1}^{N} n\, e^{-\alpha^2\omega_n^2}}{\sum_{n=1}^{N} n|T(\omega_n)|^2 e^{-\alpha^2\omega_n^2}}, \tag{4.11}$$

where $\omega_n = n\pi/L$.

We now give the quality factor of the confining potential in Eq. (4.5) as we vary particular parameters. In Fig. 4.4, we see that as we increase β, corresponding to the steepness of the interior wall of the cavity, the quality factor increases. Noting that larger β yield higher quality factors for our potential, we now analyze the quality factor for varying values of ℓ and fix the steepness to be the maximum value from Fig. 4.4.

In Fig. 4.5 we plot the quality factor as a function of the width parameter ℓ. We notice that as the width of the potential increases, so does the quality factor. This is expected if we compare our results to that of the analytic solution for the top-hat potentials. In the analytic case, we see that as the width increases the transmissivity decreases.

The results of Figs. 4.4 and 4.5 show that choosing a confining potential with $\beta = 30.0$ and $\ell = 1.0$ suffices in order to model an effective confining cavity for the short times at which we are investigating, and we will use these values for the remaining analysis.

4.2.2 Dynamical Creation of an Effective Cavity

We now switch to the analysis of the dynamical creation of the cavity from empty space without excitations. That is, we consider a scalar field theory with the time-dependent

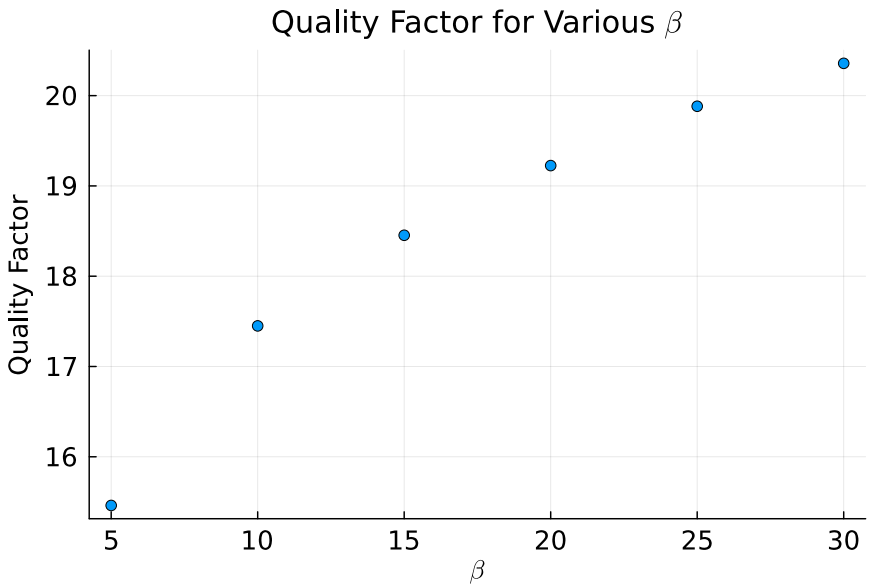

Figure 4.4: Quality factor of the confining potential as a function of β for a fixed $V_{\max} = 250$, $\ell = 1.0$, $x_{\mathrm{L}} = 3.0$, and $x_{\mathrm{R}} = 7.0$. We choose the boundaries of the cavity so that $x_{\mathrm{left}} = 2.4$ and $x_{\mathrm{right}} = 7.6$.

potential given by Eq. (4.5). We will analyze how the growth of the potential affects the energy density of the field when the field is initially in the vacuum state.

Since energy is injected into the field as the potential is created dynamically, the field will be more or less excited depending on how fast the walls are created. In Fig. 4.6 we plot the energy density at different times during the creation of a potential that is grown until $T_{\max} = 10$.

In Fig. 4.7 we again plot the energy in each particular region over time, where we see that after the potential stops growing, there is no change in energy on the interior region. Thus, as was mentioned, when the walls of the cavity are created slower, we can be assured of the effectiveness of the potential in strongly localizing the field.

Notice that a faster growing potential injects more energy into the field during its growth. As a result, higher frequency modes of the cavity become excited. One can see even in the analytical example in Eq. (4.10) that higher energy modes are more difficult to confine and thus the slower the growth of the cavity the better in confining the energy it will be. This is particularly important since, if the dynamic cavity strongly localizes the field inside the walls, then raising the walls slower will create a more effective potential.

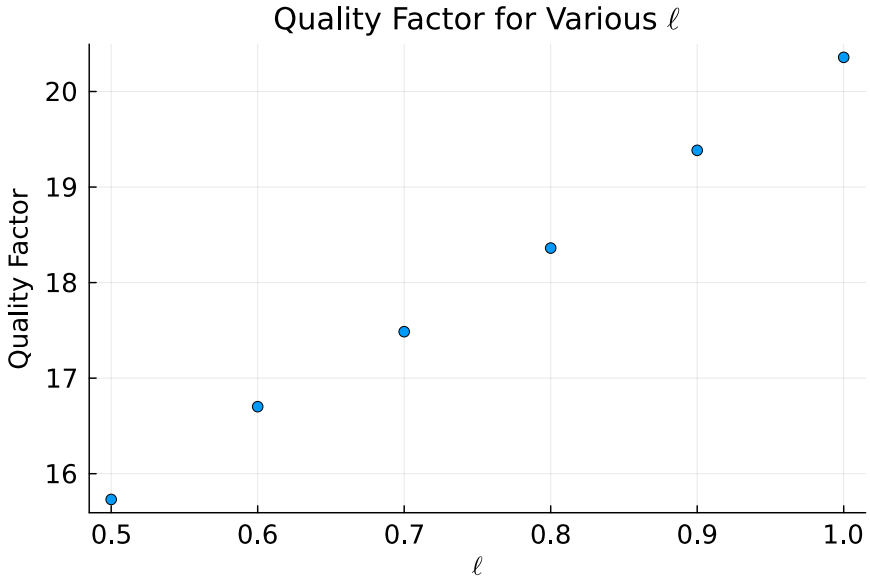

Figure 4.5: Quality factor of the confining potential as a function of ℓ (the width of the wall) for a fixed $V_{\max} = 250$, $\beta = 30.0$, $x_{\mathrm{L}} = 3.0$, and $x_{\mathrm{R}} = 7.0$. We choose the boundaries of the cavity so that $x_{\mathrm{left}} = 2.4$ and $x_{\mathrm{right}} = 7.6$.

Having established that the time-dependent potential acts as an effective cavity that confines the quantum field inside it, we can now turn our attention to the analysis of how the dynamical creation of the cavity affects the purity of the state localized and trapped inside.

4.3 Effects of the Dynamical Potential in the Mixedness of Localized Modes of the Field

Now that we have a way of dynamically localizing our free field by creating a cavity around it, the next question we investigate is that of the purity of the state of the degrees of freedom of the field trapped inside the cavity throughout the evolution. Since, before creating the potential, the vacuum state of the (free) field is a pure state, creating the cavity walls will both excite the field and introduce mixedness in the excitations that are trapped in the cavity.

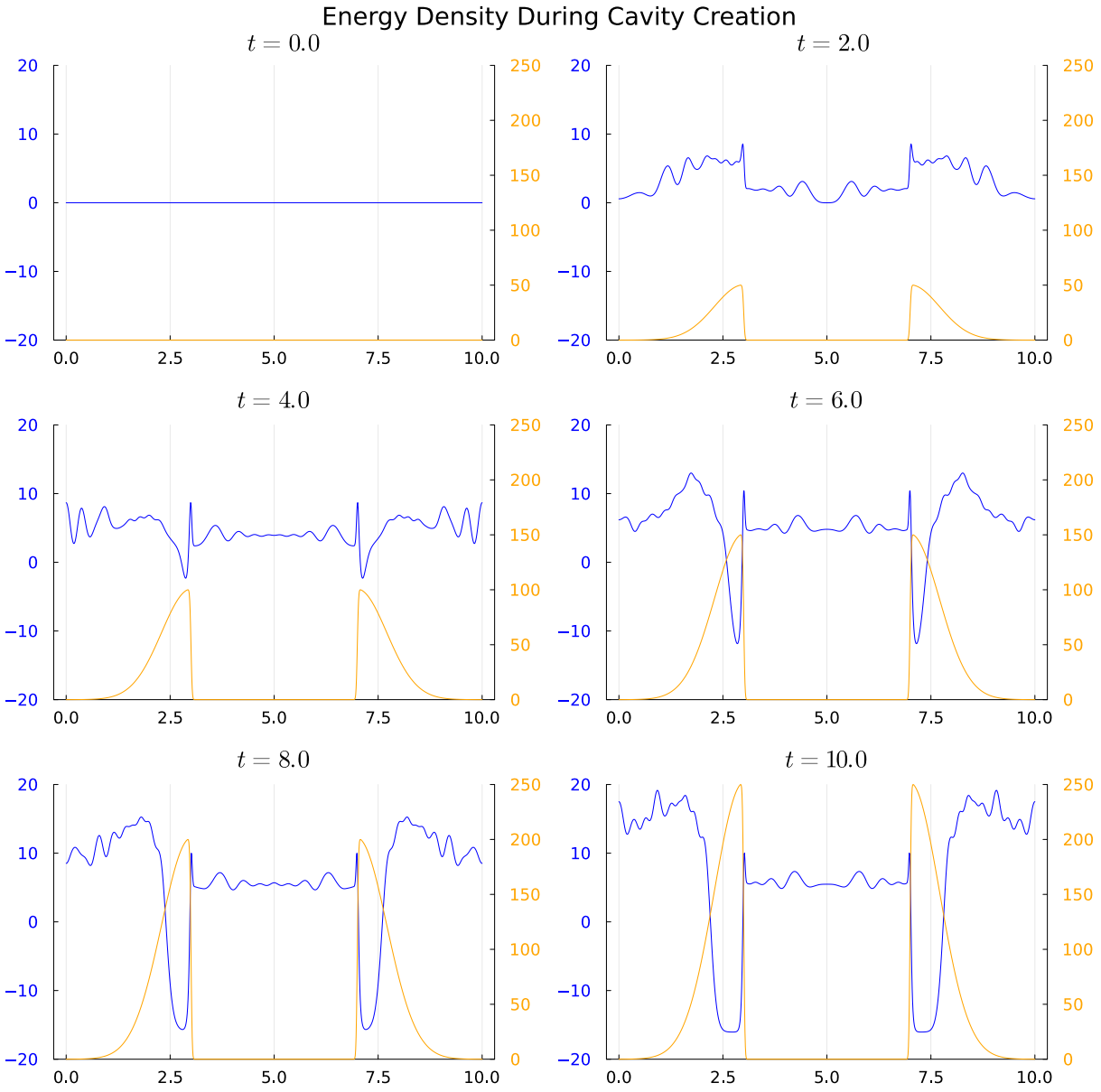

Figure 4.6: Energy density of the field during the time in which the cavity is being created. The blue curve is the energy density of the field whose value is given by the y-axis on the left of the plots, while the orange curve is the potential whose values are given by the y-axis on the right of the plots.

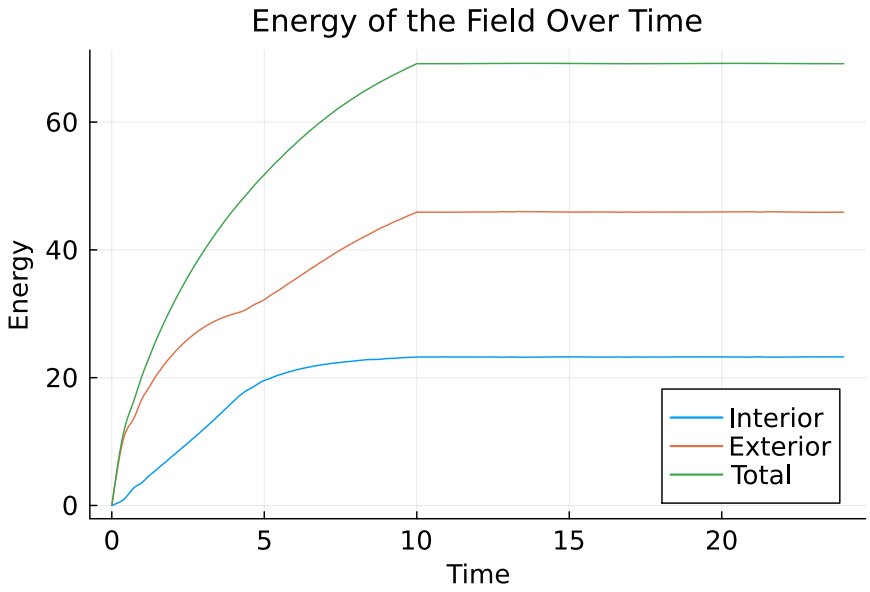

Figure 4.7: Energy of the field inside and outside of the cavity, as well as the total energy of the field as a function of time during a dynamic creation of the cavity. The potential grows up until $T_{\max} = 10$ with $V_{\max} = 250$.

Intuitively, the adiabatic theorem tells us that it should be possible to arbitrarily decrease the deviation from purity by raising the potential slower. This follows from the adiabatic theorem, in which, an adiabatically changing Hamiltonian will leave an initial ground state in the ground state of the time dependent Hamiltonian for all time. Beyond this intuition, we can actually study quantitatively the loss of purity experienced by the field modes localized inside the created cavity (when the walls are raised in the presence of the vacuum state of the field) as a function of time by first characterizing what are the degrees of freedom of the modes of the field that are localized inside the cavity. We can do so by introducing the following localized quadrature operators:

$$\hat{Q}(t) = \int \mathrm{d}x f(x)\hat{\phi}(\mathsf{x}), \tag{4.12}$$

$$\hat{P}(t) = \int \mathrm{d}x\, g(x)\hat{\Pi}(\mathsf{x}), \tag{4.13}$$

where $\hat{\Pi}(\mathsf{x}) = \partial_t\hat{\phi}(\mathsf{x})$ and $f(x)$ and $g(x)$ are the spatial profiles of the position and momentum normal modes of the cavity created by the confining potential. The functions $f(x)$

and $g(x)$ satisfy

$$\int \mathrm{d}x f(x)g(x) = 1, \tag{4.14}$$

as a result of choosing $\hat{Q}$ and $\hat{P}$ such that $\left[\hat{Q}, \hat{P}\right] = \mathrm{i}\mathbb{1}$.

Selecting a suitable profile for the quadratures requires some care. For example, it can be done by taking into account what are the actual degrees of freedom that are measurable by an experimenter, or if we know the shape of the cavity, one can reasonably choose the normal modes associated with the eigenvectors of the d'Alembert operator inside the region of confinement. Once the particular field mode and momentum mode profiles $f(x)$ and $g(x)$ are chosen, one can define the single-mode covariance matrix as

$$\sigma = \begin{pmatrix} 2\langle\hat{Q}^2\rangle & 2\mathrm{Re}\{\langle\hat{Q}\hat{P}\rangle\} \\ 2\mathrm{Re}\{\langle\hat{Q}\hat{P}\rangle\} & 2\langle\hat{P}^2\rangle \end{pmatrix}, \tag{4.15}$$

where

$$\langle\hat{Q}^2\rangle = \int \mathrm{d}x\mathrm{d}x' f(x)f(x')W(\mathsf{x},\mathsf{x}'), \tag{4.16}$$

$$\langle\hat{Q}\hat{P}\rangle = \int \mathrm{d}x\mathrm{d}x' f(x)g(x')\partial_{t'}W(\mathsf{x},\mathsf{x}'), \tag{4.17}$$

$$\langle\hat{P}^2\rangle = \int \mathrm{d}x\mathrm{d}x' g(x)g(x')\partial_t\partial_{t'}W(\mathsf{x},\mathsf{x}'). \tag{4.18}$$

Given the covariance matrix in Eq. (4.15), we define the symplectic eigenvalue of the single-mode as the positive eigenvalue of $\mathrm{i}\sigma\Omega^{-1}$, where

$$\Omega = \begin{pmatrix} 0 & 1 \\ -1 & 0 \end{pmatrix}. \tag{4.19}$$

This leads to the following expression for the symplectic eigenvalue

$$\nu(t) = 2\sqrt{\langle\hat{Q}^2(t)\rangle\langle\hat{P}^2(t)\rangle - \mathrm{Re}\{\hat{Q}(t)\hat{P}(t)\}}. \tag{4.20}$$

Using the methods of Chapter 3 to evolve the two-point correlator and the expectation of the energy density, we turn our attention to computing the symplectic eigenvalue of the selected modes of the field. The integration in Eqs. (4.16), (4.17), (4.18) is performed using a trapezoidal rule with the same grid spacing used to evolve the two-point correlator.

In order to extend the trapezoidal method used in Eq. (3.46) to a 2D integral over x, x', we can use the following recursive method for multiple integration

$$\int_{a_x}^{b_x}\int_{a_y}^{b_y} \mathrm{d}x\mathrm{d}y f(x,y) = \int_{a_x}^{b_x} \mathrm{d}x\, G(x), \tag{4.21}$$

where

$$G(x) = \int_{a_y}^{b_y} \mathrm{d}y f(x,y). \tag{4.22}$$

The result of evaluating (4.22) using the prescription (4.21) is to weight the "corner" grid points (i.e. $i = j = 0$, $i = 0, j = N_x$, $i = N_x, j = 0$, and $i = j = N_x$) by a factor of $\frac{1}{4}$, the "edge" points (i.e $i \in \{1, N_x\}, j \in [2, N_x - 1]$ and $i \in [2, N_x - 1], j \in \{1, N_x\}$) by a factor of $\frac{1}{2}$ and all interior points (i.e $i, j \in [2, N_x - 1]$) by a factor of 1. All of the necessary terms are derived and provided in Appendix C. This method is well known to be second-order convergent.

Recall that our objective is to evaluate the level of mixedness introduced in the modes of the field that remain trapped in the cavity due to its dynamical creation. To perform this analysis, we need to pick a set of modes that represent physically accessible modes inside the cavity, then analyze the state of these modes after the cavity is created after tracing out everything else.

For our particular study, we notice from Fig. 4.7 that, once the potential has stopped growing, the energy within the cavity remains constant. Therefore, to a good approximation, we can say that the resulting cavity behaves as a (fully reflecting) Dirichlet cavity. As a result, we approximate the normal modes of the cavity by the field amplitude and momentum spatial profiles as

$$f(x) = g(x) = \sqrt{\frac{2}{l}} \sin\Big(\frac{n\pi x}{l}\Big), \tag{4.23}$$

where l is the length of the artificial cavity and n corresponds to the mode number[1]. In Fig. 4.8 we show the variation in time of the symplectic eigenvalue of these effective normal modes as the cavity is created and how they behave after its creation.

In Fig. 4.8, there are quite a few interesting features. The first is that initially our symplectic eigenvalue does not equal one. This is because any localized mode of a quantum

[1]Technically the momentum profile would be multiplied by an extra power of l, however choosing the same profile for amplitude and momentum can be achieved by a single-mode squeezing which does not affect the symplectic eigenvalue calculation for this mode.

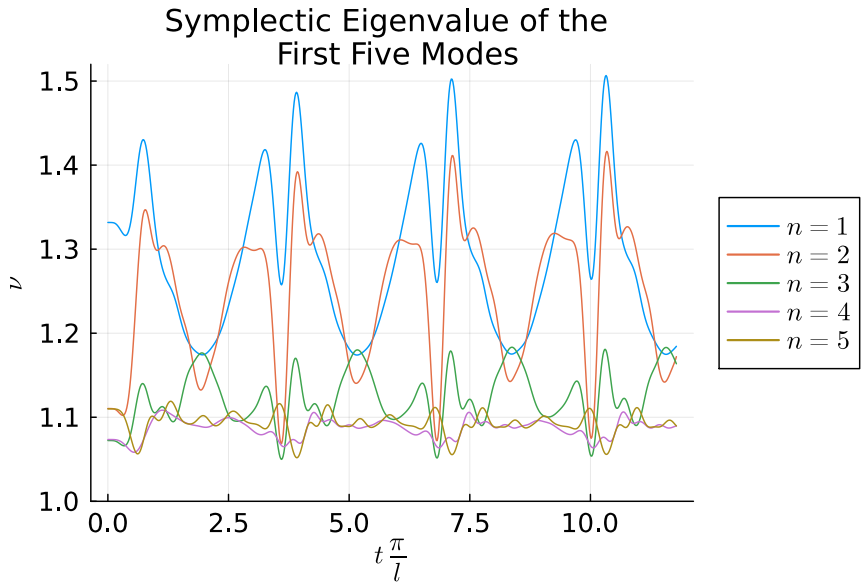

Figure 4.8: Symplectic eigenvalue for the first five modes of the field as a function of time (in units of the (inverse) fundamental frequency of the cavity). We raise the potential until $T_{\max} = 10$ and with $V_{\max} = 250$. The first mode gets more mixed because the switching is less adiabatic when the energy of the mode of study is lower.

field theory is guaranteed to be mixed, due to the inherent entanglement in the vacuum state. This means that a small amount of mixedness will always appear as a consequence of the partition into modes, even before the cavity walls are raised.

Additionally, we see that purity fluctuates throughout the evolution. In particular, we notice that the peaks are occurring at precisely one light crossing time of the artificial cavity. This is because of a combination of factors such as the fact that the modes of the cavity are not the exact normal modes for the created cavity, the fact that the potential is not infinitely confining, and the fact that the dynamical process of creating the cavity creates mixedness between the modes themselves and the outside degrees of freedom. However, as we will see later, these fluctuations do decrease as the creation of the cavity is more adiabatic. Additionally, we see that the higher modes of the artificial cavity are less mixed than the lower modes. This is due to the fact that the adiabaticity of the potential growth increases with the energy of the modes themselves. Basically, the adiabatic approximation becomes valid when $n\pi T_{\max}/l \gg 1$.

In order to fully understand the effects of the speed at which the potential grows on the mixedness of the confined degrees of freedom of the field, we ran multiple simulations

with varying values of $T_{\max}$ to analyze the results on the symplectic eigenvalue of the modes associated to the spatial profile of (4.23). As a general trend, we know that, for any given value of $T_{\max}$, the intuition one may get from the adiabatic approximation gets progressively better as we move to higher frequencies; consequently, modes with lower frequency will appear to be more mixed than the modes with higher frequency.

In Fig. 4.9, we show how the mixedness of the mode $n = 9$ varies as a function of $T_{\max}$. We choose $n = 9$ as a computational compromise: this choice allows us to see the asymptotic behavior of the purity easily within the confines of the computational resources that were available. The behavior of any other mode is expected to be similar, only the timescale at which each mode will asymptote to near purity would vary proportionally to $1/n$.

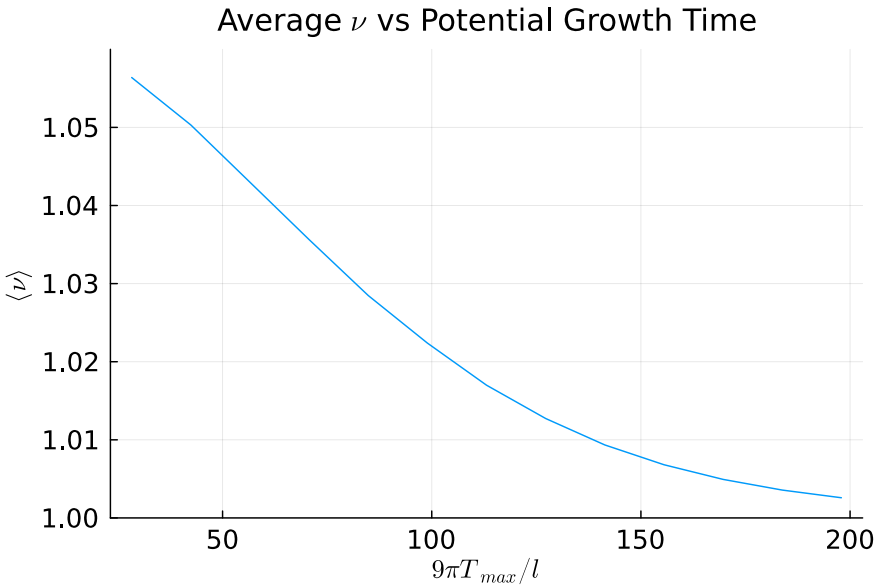

Figure 4.9: Average symplectic eigenvalue as a function of the stop time for the confining potential. Here we scale the x-axis by the frequency of the $n = 9$ mode, akin to what was done for the previous plot of the symplectic eigenvalues

The symplectic eigenvalue will oscillate as a function of time, even after the potential stops growing. For better visualization, In Fig. 4.9 we plot the time average of the symplectic eigenvalue as a function of $T_{\max}$, where the average was taken over three times the light-crossing time of the effective cavity. In this plot, we can see that as the creation of the cavity is more adiabatic, we see a monotonic decrease in the symplectic eigenvalue

that tends towards purity ($\langle\nu\rangle = 1$). This corroborates the intuition from the adiabatic theorem that if you create the cavity slowly enough, the purity of the confined modes is not compromised.

Of course, to support this claim, it is not enough to study the average in time of the symplectic eigenvalue; it is also important that its fluctuations do not go out of control. In order to evaluate these fluctuations, we can study the standard deviation of the symplectic eigenvalue $\Delta\nu = (\langle\nu^2\rangle - \langle\nu\rangle^2)^{1/2}$ as a function of T.

We show the behavior of the standard deviation in Fig. 4.10, where we see that it is small enough and also monotonically decreases as the cavity creation becomes more adiabatic. In Fig. 4.10, we also note that the standard deviation of the symplectic eigenvalue also

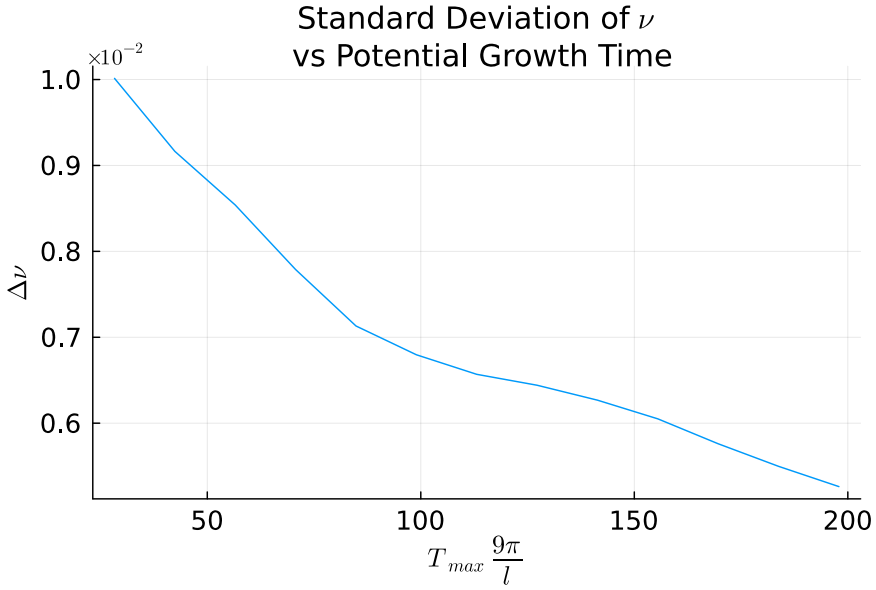

Figure 4.10: Standard deviation of the symplectic eigenvalue as a function of the stop time for the confining potential. Here we scale the x-axis by the frequency of the $n = 9$ mode.

contains purity. That is, the mode $n = 9$ that we study here obtains purity within one standard deviation of the fluctuations.

One instance where these results can be particularly useful is in a protocol known as *entanglement harvesting*. This consists of a process in which two independent localized quantum systems starting in a product state can become entangled after interacting with a quantum field. The final state of the probes after interacting with the field in this setup will generically contain contributions that can be divided into local terms (which affect

the reduced state on each detector regardless of the existence of the other), and nonlocal terms (which are responsible for the correlations between the two detectors). In rough intuitive terms, in order for the detectors to become entangled, the nonlocal correlations acquired by them should be strong enough to overcome the local terms experienced by each of them separately; in short, the nonlocal term must exceed the "local noise" on either detector. In this context, any initial mixedness in the state of the probes is detrimental to entanglement harvesting, as it effectively acts as another source of local noise that decreases the total amount of entanglement that can be potentially harvested. Therefore, in order for entanglement harvesting to be successful, it is important for the probes to be prepared in an initial state that is as pure as possible. This observation has been used to argue that particle detectors built out of modes of a relativistic quantum field have a fundamental limit to their ability to harvest entanglement at weak coupling [61], since the high level of entanglement present in the QFT describing the probe system itself inevitably leads to some level of mixedness in the initial state of the detector. Our analysis indicates, however, that the mixedness of local modes of the probe field can be made systematically smaller, if one controls the dynamics external potential that provides the localization profile of the field. This reinforces the idea of using modes of localized quantum fields as particle detectors in a way that may not be fundamentally impeded to harvest entanglement [28, 48].

Chapter 5

Conclusion and Future Work

5.1 Conclusion

In this thesis, we presented a stable and convergent FD method for evolving the correlation function of scalar quantum fields given an initial field configuration. We were able to demonstrate some example use cases for such an evolution method and how it may be optimized for different scenarios. Additionally, we showed how one can obtain the renormalized energy density of the field through only the evolution of the correlation function, again with a stable and convergent method. In doing so, we also demonstrated how this method can be optimized for efficient, long-time simulations by only considering a subset of the grid data around equal time slices $t = t'$.

The overall structure of the method developed leaves plenty of room for more general problems in $(1 + 1)$-dimensional QFT to be implemented. Moreover, the construction of this numerical method allows for simple adaptations to any linear equation of motion of a scalar quantum field. For example, with the addition of an m^2 term one can study massive scalar quantum fields, or for fields interacting with nonrelativistic sources such as particle detectors. While this method was constructed for scalar quantum fields, the overall ideas and implementations of the method can easily be extended to other quantum fields such as the fermionic field.

Specifically, we were able to adapt the numerical methods to the case where our scalar quantum field is subject to an external potential. In particular, we studied what happens when we confine degrees of freedom of a quantum field by dynamically growing cavity walls. Specifically, we focused on the study of whether the confinement introduces inescapable

mixedness in the localized degrees of freedom of the field in a way that could interfere with their use in RQI protocols, as was suggested i.e. in [61].

We showed that when we look at a confined mode with energy E of a dynamically created cavity, if the cavity is created adiabatically enough (in a timescale $T \gtrsim E^{-1}$), the confined mode does not experience significant mixedness due to the raising of the cavity walls. Moreover, the localized modes do not get significantly excited by the potential growth. This provides a proof of principle that we can obtain localized modes of the field that can be made arbitrarily pure.

One particularly important scenario where this result is relevant is the analysis of the entanglement harvesting protocol, where the mixedness of localized modes of quantum fields has been argued to be an unavoidable hindrance to one's ability to harvest entanglement with fully relativistic probes [61]. It is technically true that the Reeh-Schlieder theorem dictates that the reduced state of any local mode of a field theory in a finite region of space cannot be exactly pure unless there are regions of space where the confining potential diverges; however, our work shows that if the cavity walls are created 'slowly enough' the mixedness of localized modes of the field can be made arbitrarily negligible. To get an idea of what 'slow enough' means, we can consider, e.g., the scale of adiabaticity for an optical cavity (trapping visible light) $T \sim 10^{-15}$ s.

5.2 Future Work

In future work, it would be interesting to study the structure of the entanglement between field modes under the effect of time-dependent potentials in more detail. We expect that the mixedness observed in the modes displayed in Fig. 4.8 is mostly due to entanglement with field degrees of freedom outside of the region where the mode is supported. However, there may also be a non-trivial amount of internal entanglement among the modes within the same region of space where the cavity is being created. If this is true, then it would be possible to make an even better-informed choice of local modes via a local symplectic transformations that finds a new set of localized modes that are as uncorrelated as possible within the interior of the cavity for the specific potential that we are growing (along the lines of, e.g., [15]).

Since the primary works of this thesis were performed in $(1+1)$ dimensions, the natural next step is to utilize what we have established to create a method of evolving the correlation function of a $(3+1)$-dimensional scalar quantum field. The primary challenge is that we are unable to decrease the memory usage of storing the spatial components in

the method presented in Chapter 3. Thus, in the case of the $(3+1)$-dimensional field, this would required storing all data across a 6-dimensional array. As was mentioned in Chapter 3, this requires $\mathcal{O}(N^6)$ which is simply not feasible for high resolution simulations with our current computational resources. As of the completion of this thesis, progress has been made in utilizing the methods of [78, 26] to decrease the memory usage to a factor of $\mathcal{O}(N\log(N^5))$. Currently, these methods are being adapted in order to perform the necessary time integration to generate the full time dynamics of the correlation function in $(3+1)$-dimensions.

With a $(3+1)$-dimensional simulation, there are also a number of protocols in RQI that can be studied in a more realistic, less idealized scenario. An obvious example of this would be to study the dynamic localization of a $(3+1)$-dimensional scalar quantum field. Additionally, one could study a scenario where the protocol of entanglement harvesting uses a dynamically localized quantum field as a particle detector, building on the works of [49, 50].

Outside of the case of a $(3+1)$-dimensional numerical method, the current $(1+1)$-dimensional code can be used to replicate idealized studies in QFT (see e.g. [8]) with parameters that are more akin to what an experimental research group has access to in a laboratory. This could lead to developing an understanding of what may be necessary in order for experiments to confirm theoretical works in QFT.

Additionally, given the limited literature in the area of numerical QFT, there is a, potentially, interesting analogue between that of a bandlimited QFT and the use of discrete derivatives (such as those used in Chapter 3). A bandlimited theory is inherently not covariant, but is still a method of discretization that preserves Lorentz symmetry. Understanding the way in which these two ideas are the same (or perhaps how the differ), could lead to developing numerical methods for QFT that are in-line with our current framework for QFT.

The most, in my personal opinion, interesting project that can build upon these works, is obtaining the full renormalized, stress-energy tensor $\langle\hat{T}_{\mu\nu}\rangle$ of the field. The main point of interest in numerically obtaining the stress-energy tensor is that this is precisely the source term of the Einstein Field Equations. That is, if one can give the stress-energy tensor, then it is possible, using techniques from numerical relativity, to solve the Einstein Field Equations for a full simulation of the backreaction on a scalar quantum field. This could provide huge insights into the interplay between QFT and general relativity allowing us to have a better understanding of the gravitation of quantum fields in the weak field limit.

References

[1] Miguel Alcubierre. *Introduction to 3+1 Numerical Relativity*. Oxford University Press, 04 2008.

[2] Kendall E. Atkinson. *An Introduction to Numerical Analysis*. Wiley, 1991.

[3] Jakob A. Bærentzen, Jens Gravesen, François Anton, and Henrik Aanæs. *Guide to Computational Geometry Processing*. Springer London, 2012.

[4] Jeff Bezanson, Alan Edelman, Stefan Karpinski, and Viral B Shah. Julia: A fresh approach to numerical computing. *SIAM review*, 59(1):65–98, 2017.

[5] N. D. Birrell and P. C. W. Davies. *Quantum Fields in Curved Space*. Cambridge Monographs on Mathematical Physics. Cambridge University Press, 1982.

[6] Ana Blasco, Luis J. Garay, Mercedes Martín-Benito, and Eduardo Martín-Martínez. Violation of the strong huygen's principle and timelike signals from the early universe. *Phys. Rev. Lett.*, 114:141103, Apr 2015.

[7] Tom Breloff. Plots.jl, November 2024.

[8] Eric G. Brown, Marco del Rey, Hans Westman, Juan León, and Andrzej Dragan. What does it mean for half of an empty cavity to be full? *Physical Review D*, 91(1), January 2015.

[9] P. Candelas and D. W. Sciama. Irreversible thermodynamics of black holes. *Phys. Rev. Lett.*, 38:1372–1375, Jun 1977.

[10] Jiahao Chen and Jarrett Revels. Robust benchmarking in noisy environments. *arXiv e-prints*, Aug 2016.

[11] S. M. Christensen. Vacuum expectation value of the stress tensor in an arbitrary curved background: The covariant point-separation method. *Phys. Rev. D*, 14:2490–2501, Nov 1976.

[12] S. M. Christensen. Regularization, renormalization, and covariant geodesic point separation. *Phys. Rev. D*, 17:946–963, Feb 1978.

[13] M. Cliche and A. Kempf. Relativistic quantum channel of communication through field quanta. *Phys. Rev. A*, 81:012330, Jan 2010.

[14] José de Ramón, Maria Papageorgiou, and Eduardo Martín-Martínez. Relativistic causality in particle detector models: Faster-than-light signaling and impossible measurements. *Phys. Rev. D*, 103:085002, Apr 2021.

[15] Bruno de S. L. Torres, Kelly Wurtz, José Polo-Gómez, and Eduardo Martín-Martínez. Entanglement structure of quantum fields through local probes. *J. High Energy Phys.*, 2023(5):58, May 2023.

[16] David Del Rey Fernández, Jason Hicken, and David Zingg. Review of summation-by-parts operators with simultaneous approximation terms for the numerical solution of partial differential equations. *Computers and Fluids*, 95:171–196, 05 2014.

[17] B. DeWitt. *General Relativity; an Einstein Centenary Survey*. Cambridge University Press, Cambridge, UK, 1980.

[18] Christopher J. Fewster. A generally covariant measurement scheme for quantum field theory in curved spacetimes, 2019.

[19] Christopher J. Fewster and Kasia Rejzner. Algebraic quantum field theory – an introduction, 2019.

[20] Christopher J Fewster and Rainer Verch. The necessity of the hadamard condition. *Classical and Quantum Gravity*, 30(23):235027, November 2013.

[21] Christopher J. Fewster and Rainer Verch. Quantum fields and local measurements, 2018.

[22] Christopher J. Fewster and Rainer Verch. Measurement in quantum field theory. In Richard Szabo and Martin Bojowald, editors, *Encyclopedia of Mathematical Physics (Second Edition)*, pages 335–345. Academic Press, Oxford, second edition edition, 2025.

[23] Joshua Foo, Robert B. Mann, and Magdalena Zych. Entanglement amplification between superposed detectors in flat and curved spacetimes. *Phys. Rev. D*, 103:065013, Mar 2021.

[24] S.A Fulling, F.J Narcowich, and Robert M Wald. Singularity structure of the two-point function in quantum field theory in curved spacetime, ii. *Annals of Physics*, 136(2):243–272, 1981.

[25] Stephen A. Fulling, Mark Sweeny, and Robert M. Wald. Singularity structure of the two-point function in quantum field theory in curved spacetime. *Comm. Math. Phys*, 63:257–264, 1978.

[26] Jochen Garcke. Sparse grids in a nutshell. In Jochen Garcke and Michael Griebel, editors, *Sparse Grids and Applications*, pages 57–80, Berlin, Heidelberg, 2013. Springer Berlin Heidelberg.

[27] I. S. Gradshteyn and I. M. Ryzhik. *Table of integrals, series, and products*. Elsevier/Academic Press, Amsterdam, seventh edition, 2007.

[28] Daniel Grimmer, Bruno de S. L. Torres, and Eduardo Martín-Martínez. Measurements in qft: Weakly coupled local particle detectors and entanglement harvesting. *Phys. Rev. D*, 104:085014, Oct 2021.

[29] K. E. Hellwig and K. Kraus. Formal description of measurements in local quantum field theory. *Phys. Rev. D*, 1:566–571, Jan 1970.

[30] Laura J. Henderson, Su Yu Ding, and Robert B. Mann. Entanglement harvesting with a twist, 2022.

[31] Laura J Henderson, Robie A Hennigar, Robert B Mann, Alexander R H Smith, and Jialin Zhang. Harvesting entanglement from the black hole vacuum. *Class. Quantum Gravity*, 35(21):21LT02, oct 2018.

[32] Francis E. Hildebrand. *Introduction to Numerical Analysis*. McGraw-Hill, 2nd edition, 1987.

[33] Robert H. Jonsson, Eduardo Martín-Martínez, and Achim Kempf. Information transmission without energy exchange. *Phys. Rev. Lett.*, 114:110505, Mar 2015.

[34] Benito A. Juárez-Aubry, Tonatiuh Miramontes, and Daniel Sudarsky. Semiclassical theories as initial value problems. *Journal of Mathematical Physics*, 61(3), 2020.

[35] Bernard S. Kay and Robert M. Wald. Theorems on the uniqueness and thermal properties of stationary, nonsingular, quasifree states on spacetimes with a bifurcate killing horizon. *Physics Reports*, 207(2):49–136, 1991.

[36] André G. S. Landulfo. Nonperturbative approach to relativistic quantum communication channels. *Phys. Rev. D*, 93:104019, May 2016.

[37] H.P. Langtangen and S. Linge. *Finite Difference Computing with PDEs*. Texts in Computational Science and Engineering. Springer Cham, 2017.

[38] R.J. LeVeque. *Finite Difference Methods for Ordinary and Partial Differential Equations: Steady-State and Time-Dependent Problems*. Other Titles in Applied Mathematics. Society for Industrial and Applied Mathematics, 2007.

[39] Richard Lopp and Eduardo Martín-Martínez. Quantum delocalization, gauge, and quantum optics: Light-matter interaction in relativistic quantum information. *Phys. Rev. A*, 103:013703, Jan 2021.

[40] Jorma Louko and Alejandro Satz. How often does the unruh–dewitt detector click? regularization by a spatial profile. *Classical and Quantum Gravity*, 23(22):6321, oct 2006.

[41] Eduardo Martín-Martínez. Causality issues of particle detector models in QFT and quantum optics. *Phys. Rev. D*, 92:104019, Nov 2015.

[42] Eduardo Martín-Martínez, T. Rick Perche, and Bruno de S. L. Torres. Broken covariance of particle detector models in relativistic quantum information. *Phys. Rev. D*, 103:025007, Jan 2021.

[43] Eduardo Martín-Martínez, Boris Ragula, Erik Schnetter, and Bruno de S. L. Torres. A finite difference method for numerically evolving correlation functions of scalar quantum fields, In preparation.

[44] Diana Mendez-Avalos, Laura J. Henderson, Kensuke Gallock-Yoshimura, and Robert B. Mann. Entanglement harvesting of three unruh-dewitt detectors. *Gen. Relativ. and Gravit.*, 54(8):87, Aug 2022.

[45] M.E.J. Newman. *Computational Physics*. CreateSpace Independent Publishing Platform, 2013.

[46] Maria Papageorgiou and Doreen Fraser. Eliminating the "impossible": Recent progress on local measurement theory for quantum field theory, 2023.

[47] T. Rick Perche and Eduardo Martín-Martínez. Geometry of spacetime from quantum measurements. *Phys. Rev. D*, 105:066011, Mar 2022.

[48] T. Rick Perche, José Polo-Gómez, Bruno de S. L. Torres, and Eduardo Martín-Martínez. Fully relativistic entanglement harvesting. *Phys. Rev. D*, 109:045018, Feb 2024.

[49] T. Rick Perche, José Polo-Gómez, Bruno de S. L. Torres, and Eduardo Martín-Martínez. Particle detectors from localized quantum field theories. *Phys. Rev. D*, 109:045013, Feb 2024.

[50] T. Rick Perche, José Polo-Gómez, Bruno de S.L. Torres, and Eduardo Martín-Martínez. Fully relativistic entanglement harvesting. *Physical Review D*, 109(4), February 2024.

[51] T. Rick Perche, Boris Ragula, and Eduardo Martín-Martínez. Harvesting entanglement from the gravitational vacuum, 2022.

[52] José Polo-Gómez, Luis J. Garay, and Eduardo Martín-Martínez. A detector-based measurement theory for quantum field theory. *Phys. Rev. D*, 105:065003, Mar 2022.

[53] Alejandro Pozas-Kerstjens, Jorma Louko, and Eduardo Martín-Martínez. Degenerate detectors are unable to harvest spacelike entanglement. *Phys. Rev. D*, 95:105009, May 2017.

[54] Alejandro Pozas-Kerstjens and Eduardo Martín-Martínez. Harvesting correlations from the quantum vacuum. *Phys. Rev. D*, 92:064042, Sep 2015.

[55] Alejandro Pozas-Kerstjens and Eduardo Martín-Martínez. Entanglement harvesting from the electromagnetic vacuum with hydrogenlike atoms. *Phys. Rev. D*, 94:064074, Sep 2016.

[56] Boris Ragula. Slab optimized evolution of correlation functions, minkowski spacetime. https://github.com/bragulaET/CorrelationFunctions/tree/main, 2024.

[57] Boris Ragula, Erik Schnetter, and Eduardo Martín-Martínez. A finite difference method for numerically evolving correlation functions of scalar quantum fields, In preparation.

[58] M. Redhead. More ado about nothing. *Found Phys*, 25:123–137, 1995.

[59] H. Reeh and S. Schlieder. Bemerkungen zur unitäräquivalenz von lorentzinvarianten feldern. *Nuovo Cim*, 22:1051–1068, 1961.

[60] Benni Reznik, Alex Retzker, and Jonathan Silman. Violating bell's inequalities in vacuum. *Phys. Rev. A*, 71(4):042104, 2005.

[61] Maximilian H Ruep. Weakly coupled local particle detectors cannot harvest entanglement. *Classical and Quantum Gravity*, 38(19):195029, sep 2021.

[62] S. Schlieder. Einige bemerkungen zur zustandsänderung von relativistischen quantenmechanischen systemen durch messungen und zur lokalitätsforderung. *Comm. Math. Phys*, 7:305–331, 1968.

[63] J. Silman and B. Reznik. Long-range entanglement in the Dirac vacuum. *Phys. Rev. A*, 75:052307, 2007.

[64] Petar Simidzija, Aida Ahmadzadegan, Achim Kempf, and Eduardo Martín-Martínez. Transmission of quantum information through quantum fields. *Phys. Rev. D*, 101:036014, Feb 2020.

[65] R D Sorkin. Expressing entropy globally in terms of (4d) field-correlations. *Journal of Physics: Conference Series*, 484(1):012004, mar 2014.

[66] Rafael D. Sorkin. From green function to quantum field. *International Journal of Geometric Methods in Modern Physics*, 14(08):1740007, 2017.

[67] Rafael D Sorkin and Yasaman K Yazdi. Entanglement entropy in causal set theory. *Classical and Quantum Gravity*, 35(7):074004, mar 2018.

[68] John C. Strikwerda. *Finite Difference Schemes and Partial Differential Equations, Second Edition*. Society for Industrial and Applied Mathematics, 2nd edition, 2004.

[69] J. W. Thomas. *Numerical Partial Differential Equations: Finite Difference Methods*. Springer New York, NY, 1995.

[70] Erickson Tjoa and Kensuke Gallock-Yoshimura. Channel capacity of relativistic quantum communication with rapid interaction. *Phys. Rev. D*, 105:085011, Apr 2022.

[71] Bruno de S. L. Torres. Particle detector models from path integrals of localized quantum fields. *Phys. Rev. D*, 109:065004, Mar 2024.

[72] W. G. Unruh. Notes on black-hole evaporation. *Phys. Rev. D*, 14:870–892, Aug 1976.

[73] Antony Valentini. Non-local correlations in quantum electrodynamics. *Phys. Lett. A*, 153(6-7):321 – 325, 1991.

[74] Robert Manuel Wald. *Quantum Field Theory in Curved Spacetime and Black Hole Thermodynamics*. The University of Chicago Press, 1994.

[75] D. Wang, S. Appelö and G. Kreiss. An energy-based summation-by-parts finite difference method for the wave equation in second order form. *Journal of Scientific Computing*, 91, 2022.

[76] Barry Wardell, Chad R. Galley, Anı l Zenginoğlu, Marc Casals, Sam R. Dolan, and Adrian C. Ottewill. Self-force via green functions and worldline integration. *Phys. Rev. D*, 89:084021, Apr 2014.

[77] Steven Weinberg. *The Quantum Theory of Fields*. Cambridge University Press, 1995.

[78] C. Zenger. Sparse grids. In W. Hackbusch, editor, *Notes on Numerical Fluid Mechanics*, pages 241–251. Vieweg, Braunschweig, Wiesbaden, vol. 31 edition, 1991.

[79] Anı l Zenginoğlu and Chad R. Galley. Caustic echoes from a schwarzschild black hole. *Phys. Rev. D*, 86:064030, Sep 2012.

APPENDICES

Appendix A

Appendices for Chapter 2

A.1 Equal Time Commutation Relations Imply Canonical Commutation Relations

Before demonstrating the equivalence between the equal time commutation relations and the canonical commutation relations, we first mention that we will be demonstrating this relationship using the cavity QFT formalism. This is mainly because the cavity results are used in all chapters of the thesis. That being said, the calculation is almost identical in the case of a free QFT. We will also make use of the following two important results,

$$(\hat{\phi}(\mathsf{x}), u_{k_n}(\mathsf{x}))_{\text{K.G.}} = \hat{a}_{k_n}, \tag{A.1}$$

$$(\hat{\phi}(\mathsf{x}), u^*_{k_n}(\mathsf{x}))_{\text{K.G.}} = \hat{a}^\dagger_{k_n}, \tag{A.2}$$

which can easily be shown using the orthogonality of the basis functions $\{u_{k_n}(\mathsf{x})\}$ under the Klein-Gordon inner product.

The first two commutation relations, namely Eqs. (2.30) and (2.31) are quite clear from the definitions of the equal time commutation relations. However, the third is slightly more

nuanced and can be seen through the following calculation

$$\begin{aligned}
&\left[\hat{a}_{k_n}, \hat{a}^\dagger_{k_n}\right] = \langle\hat{\phi}(x,t), u_{k_n}(x,t)\rangle\langle\hat{\phi}(x,t), u^*_{k_m}(x,t)\rangle - \langle\hat{\phi}(x,t), u^*_{k_m}(x,t)\rangle\langle\hat{\phi}(x,t), u_{k_n}(x,t)\rangle \\
&= -\int_0^L \mathrm{d}x\mathrm{d}x' \left[\hat{\phi}(x,t)(\partial_t u_{k_n}(x,t)) - \hat{\Pi}(x,t)u_{k_n}(x,t)\right]\left[\hat{\phi}(x',t)(\partial_t u^*_{k_m}(x',t)) - \hat{\Pi}(x',t)u^*_{k_m}(x',t)\right] \\
&- \left(-\int_0^L \mathrm{d}x\mathrm{d}x' \left[\hat{\phi}(x',t)(\partial_t u^*_{k_m}(x',t)) - \hat{\Pi}(x',t)u^*_{k_m}(x',t)\right]\left[\hat{\phi}(x,t)(\partial_t u_{k_n}(x,t)) - \hat{\Pi}(x,t)u_{k_n}(x,t)\right]\right) \\
&= \int_0^L \mathrm{d}x\mathrm{d}x' \Big[\hat{\phi}(x,t), \hat{\Pi}(x',t)\Big](\partial_t u_{k_n}(x,t))u^*_{k_m}(x',t) + \Big[\hat{\Pi}(x,t), \hat{\phi}(x',t)\Big](\partial_t u^*_{k_m}(x',t))u_{k_n}(x,t) \\
&= \mathrm{i}\int_0^L \delta(x-x')\left((\partial_t u_{k_n}(x,t))u^*_{k_m}(x',t) - (\partial_t u^*_{k_m}(x',t))u_{k_n}(x,t)\right) \\
&= \left(\frac{k_n}{\pi\sqrt{nm}} + \frac{k_m}{\pi\sqrt{nm}}\right) e^{-\mathrm{i}(k_n-k_m)t}\int_0^L \mathrm{d}x \sin\frac{n\pi x}{L}\sin\Big(\frac{m\pi x}{L}\Big). \qquad \text{(A.3)}
\end{aligned}$$

In the above equation, if $n \neq m$, then $\left[\hat{a}_{k_n}, \hat{a}^\dagger_{k_m}\right] = 0$, and if $n = m$, then $\left[\hat{a}_{k_n}, \hat{a}^\dagger_{k_m}\right] = 1$, thus we conclude that $\left[\hat{a}_{k_n}, \hat{a}^\dagger_{k_m}\right] = \delta_{nm}$. Thus we conclude that Eq. (2.32) is also naturally imposed by the equal time commutation relations.

A.2 Derivation of the Vacuum Correlation Function

Starting from the definition of the correlation function in Eq. (2.33), we have

$$\begin{aligned}
W_0(\mathsf{x},\mathsf{x}') &= \langle 0|\,\hat{\phi}(\mathsf{x})\hat{\phi}(\mathsf{x}')\,|0\rangle \\
&= \langle 0|\left(\int \mathrm{d}^n\boldsymbol{k}\left(\hat{a}_{\boldsymbol{k}}u_{\boldsymbol{k}}(\mathsf{x}) + \hat{a}^\dagger_{\boldsymbol{k}}u^*_{\boldsymbol{k}}(\mathsf{x})\right)\int \mathrm{d}^n\boldsymbol{k}'\left(\hat{a}_{\boldsymbol{k}'}u_{\boldsymbol{k}'}(\mathsf{x}') + \hat{a}^\dagger_{\boldsymbol{k}'}u^*_{\boldsymbol{k}'}(\mathsf{x}')\right)\right)|0\rangle\,. \qquad \text{(A.4)}
\end{aligned}$$

From here, given the orthogonality relations, any terms in Eq. (A.4) that contain unequal numbers of creation and annihilation operators will be zero. So we obtain

$$W_0(\mathsf{x},\mathsf{x}') = \int \mathrm{d}^n\boldsymbol{k}\mathrm{d}^n\boldsymbol{k}'\,\langle 0|\left(\hat{a}_{\boldsymbol{k}}\hat{a}^\dagger_{\boldsymbol{k}'}u_{\boldsymbol{k}}(\mathsf{x})u^*_{\boldsymbol{k}'}(\mathsf{x}') + \hat{a}^\dagger_{\boldsymbol{k}}\hat{a}_{\boldsymbol{k}'}u^*_{\boldsymbol{k}}(\mathsf{x})u_{\boldsymbol{k}'}(\mathsf{x}')\right)|0\rangle\,. \qquad \text{(A.5)}$$

Since $\hat{a}_{\boldsymbol{k}} |0\rangle = 0$, we have

$$\begin{aligned} W_0(\mathsf{x}, \mathsf{x}') &= \int \mathrm{d}^n \boldsymbol{k} \mathrm{d}^n \boldsymbol{k}' \, \langle 0| \, \hat{a}_{\boldsymbol{k}} \hat{a}^\dagger_{\boldsymbol{k}'} \, |0\rangle \, u_{\boldsymbol{k}}(\mathsf{x}) u^*_{\boldsymbol{k}'}(\mathsf{x}') \\ &= \int \mathrm{d}^n \boldsymbol{k} \mathrm{d}^n \boldsymbol{k}' \, \langle 0| \left(\delta^{(n)}(\boldsymbol{k} - \boldsymbol{k}') - \hat{a}^\dagger_{\boldsymbol{k}'} \hat{a}_{\boldsymbol{k}} \right) |0\rangle \, u_{\boldsymbol{k}}(\mathsf{x}) u^*_{\boldsymbol{k}'}(\mathsf{x}') \\ &= \int \mathrm{d}^n \boldsymbol{k} \, u_{\boldsymbol{k}}(\mathsf{x}) u^*_{\boldsymbol{k}}(\mathsf{x}'), \end{aligned} \tag{A.6}$$

where we used the fact that $\langle 0|0\rangle = 1$, and again used the fact that $\hat{a}_{\boldsymbol{k}} |0\rangle = 0$. Substituting in Eq. (2.12), we obtain

$$W_0(\mathsf{x}, \mathsf{x}') = \int \frac{\mathrm{d}^n \boldsymbol{k}}{(2\pi)^n 2\omega_{\boldsymbol{k}}} e^{\mathrm{i} k_\mu (x - x')^\mu}. \tag{A.7}$$

Appendix B

Appendices for Chapter 3

B.1 Derivation of the CFL Condition for the Wave Equation

We can derive the CFL condition for the wave equation by first inserting the Fourier decomposition of our error Eq. (3.15) into our FD method in Eq. 3.5. In doing so, we obtain

$$\begin{aligned} \hat{e}_{n+1}e^{ij\theta} &= 2\hat{e}_n e^{ij\theta} - \hat{e}_{n-1}e^{ij\theta} + C^2\left(\hat{e}_n e^{i(j+1)\theta} - 2\hat{e}_n e^{ij\theta} + \hat{e}_n e^{i(j-1_\theta}\right) \\ \hat{e}_{n+1} + \hat{e}_{n-1} &= \hat{e}_n\left(2 + 2C^2\cos(\theta) - 2C^2\right). \end{aligned} \tag{B.1}$$

In order to ensure the stability of the method, we now assume $\hat{e}_n = \lambda^n$. It can be shown that Eq. (3.16) implies that, for our method to be stable, we require $|\lambda| \leq 1$. Under this assumption we have,

$$\lambda^2 - M\lambda + 1 = 0, \tag{B.2}$$

where

$$M = 2 + 2R^2\cos(\theta) - 2R^2. \tag{B.3}$$

The roots of Eq. (B.2) are then

$$\lambda_{1,2} = \frac{M}{2} \pm \frac{1}{2}\sqrt{M^2 - 4}. \tag{B.4}$$

If we assume that $M^2 - 4 > 0$, then we must have $M < -2$ since $M \leq 2$, which yields $\lambda_2 < -1 \implies |\lambda_2| > 1$ which would result in our method being unstable. So we must have

that $M^2 - 4 \leq 0$ and the roots become

$$\begin{aligned}
\lambda_{1,2} &= \frac{M}{2} \pm \frac{\mathrm{i}}{2}\sqrt{4 - M^2} \\
&\implies |\lambda_{1,2}| = \sqrt{\frac{M^2}{4} + \frac{4 - M^2}{4}} \leq 1 \\
&\iff M^2 - 4 \leq 0 \\
&\implies -2 \leq M \leq 2.
\end{aligned} \tag{B.5}$$

In other words, we have the condition

$$-2 \leq 2 + 2R^2\cos(\theta) - 2R^2 \leq 2. \tag{B.6}$$

Now we can start by analyzing the case where $M \leq 2$ and what restrictions this may impose.

$$\begin{aligned}
2 + 2R^2\cos(\theta) - 2R^2 &\leq 2 \\
R^2\cos(\theta) - R^2 &\leq 0 \\
\frac{1}{\Delta x^2}(\cos(\theta) - 1) &\leq 0,
\end{aligned} \tag{B.7}$$

which will always be satisfied. We must also satisfy the other side of the equality, which will indeed impose additional restrictions on the size of the time step we may use for the simulation.

$$\begin{aligned}
-2 &\leq 2 + 2R^2\cos(\theta) - 2R^2 \\
-4 &\leq 2R^2(\cos(\theta) - 1) \leq -4R^2 \\
4 &\geq 4R^2.\Delta t \leq \Delta x
\end{aligned} \tag{B.8}$$

Thus, we have arrived at the stability condition given in Eq. (3.17).

B.2 Derivation of the Regularized Correlation Function

Starting from Eq. (3.23), we substitute Eqs. (2.42), (3.21), and (3.22) and we obtain

$$\begin{aligned}\mathcal{W}_0(\mathsf{x},\mathsf{x}') = \frac{1}{\pi}\sum_{n=1}^{\infty}\frac{1}{n}&\left(\frac{1}{\sqrt{2\pi\sigma_x^2}}\int \mathrm{d}y\,\sin(k_n y)e^{-(x-y)^2/2\sigma_x^2}\right)\\ &\times\left(\frac{1}{\sqrt{2\pi\sigma_x^2}}\int \mathrm{d}y'\,\sin(k_n y')e^{-(x'-y')^2/2\sigma_x^2}\right)\left(\frac{1}{\sqrt{2\pi\sigma_t^2}}\int \mathrm{d}\tau e^{-\mathrm{i}k_n\tau}e^{-(t-\tau)^2}\right)\\ &\times\left(\frac{1}{\sqrt{2\pi\sigma_t^2}}\int \mathrm{d}\tau' e^{-\mathrm{i}k_n\tau'}e^{-(t'-\tau')^2}\right)\end{aligned} \tag{B.9}$$

All of the integrals can be evaluated analytically and are found in [27]. We first solve the integral in y and will note that the integral in y' has the same result.

$$\begin{aligned}\frac{1}{\sqrt{2\pi\sigma_x^2}}\int \mathrm{d}y\,\sin(k_n y)e^{-(x-y)^2/2\sigma_x^2} &= \frac{1}{\sqrt{2\pi\sigma_x^2}}\int \mathrm{d}u\,\sin(k_n(u+x))e^{-u^2/2\sigma_x^2}\\ &= e^{-\frac{1}{2}k_n^2\sigma_x^2}\sin(k_n x).\end{aligned} \tag{B.10}$$

Similarly, the result for the second integral is given by

$$\frac{1}{\sqrt{2\pi\sigma_x^2}}\int \mathrm{d}y'\,\sin(k_n y')e^{-(x'-y')^2/2\sigma_x^2} = e^{-\frac{1}{2}k_n^2\sigma_x^2}\sin(k_n x'). \tag{B.11}$$

For the third integral, we have

$$\begin{aligned}\frac{1}{\sqrt{2\pi\sigma_t^2}}\int \mathrm{d}\tau e^{-\mathrm{i}k_n\tau}e^{-(t-\tau)^2/2\sigma_t^2} &= \frac{e^{-\mathrm{i}k_n t}}{\sqrt{2\pi\sigma_t^2}}\int \mathrm{d}u e^{-\mathrm{i}k_n u}e^{-u^2/2\sigma_t^2}\\ &= \frac{e^{-\mathrm{i}k_n t}}{\sqrt{2\pi\sigma_t^2}}\left(\int \mathrm{d}u\cos(k_n u)e^{-u^2/2\sigma_t^2} - \mathrm{i}\int \mathrm{d}u\sin(k_n u)e^{-u^2/2\sigma_t^2}\right)\\ &= e^{-\mathrm{i}k_n t}\left(e^{-\frac{1}{2}k_n^2\sigma_t^2}\cos(k_n * 0) - \mathrm{i}e^{-\frac{1}{2}k_n^2\sigma_t^2}\sin(k_n * 0)\right)\\ &= e^{-\mathrm{i}k_n t}e^{-\frac{1}{2}k_n^2\sigma_t^2}\end{aligned} \tag{B.12}$$

Finally, for the fourth integral, we notice that this integral is simply the complex conjugate of the above the integral. Thus, we obtain

$$\frac{1}{\sqrt{2\pi\sigma_t^2}}\int \mathrm{d}\tau' e^{-\mathrm{i}k_n\tau'}e^{-(t'-\tau')^2/2\sigma_t^2} = e^{\mathrm{i}k_n t'}e^{-\frac{1}{2}k_n^2\sigma_t^2} \tag{B.13}$$

Substituting the results of the above integrals yields the result of Eq. (3.24).

Appendix C

Appendices for Chapter 4

C.1 Derivation of the CFL Condition for the Wave Equation With External Potential

The derivation for the CFL Factor for the wave equation with an external potential is similar to that of the wave equation without a potential. As we will see, the derivation relies heavily on the same techniques used in B.

Upon substituting Eq. (3.15) into the discretized version of Eq. (4.2), we obtain

$$\hat{e}_{n+1}e^{ij\theta} = 2\hat{e}_n e^{ij\theta} - \hat{e}_{n-1}e^{ij\theta} + R^2\left(\hat{e}_n e^{i(j+1)\theta} - 2\hat{e}_n e^{ij\theta} + \hat{e}_n e^{i(j-1)\theta}\right) - 2\Delta t^2 V_i^n \hat{e}_n e^{ij\theta},$$

which yields

$$\hat{e}_{n+1} + \hat{e}_{n-1} = \hat{e}_n(2 + 2R^2\cos(\theta) - 2R^2 - 2\Delta t^2 V_i^n) \tag{C.1}$$

As before, we will assume $\hat{e}_n = \lambda^n$ and require that $|\lambda| \leq 1$. Under this assumption, we again get a quadratic equation of the form

$$\lambda^2 - M\lambda + 1 = 0, \tag{C.2}$$

where

$$M = 2 + 2R^2\cos(\theta) - 2R^2 - 2\Delta t^2 V_i^n. \tag{C.3}$$

To further simplify the equation, we define $\tilde{V} = max_{\{n,i\}\in\mathcal{D}} V_i^n$, and noting that $\tilde{V} \geq 0$

we arrive at the following result for the roots of λ

$$\lambda_{1,2} = \frac{M}{2} \pm \frac{1}{2}\sqrt{M^2 - 4}. \tag{C.4}$$

If we assume that $M^2 - 4 > 0$, then we must have $M < -2$ since $M \leq 2 + 2\Delta t^2 \tilde{V}$, which yields $\lambda_2 < -1 \implies |\lambda_2| > 1$ which would result in our method being unstable. So we must have that $M^2 - 4 \leq 0$ and the roots become

$$\begin{aligned} \lambda_{1,2} &= \frac{M}{2} \pm \frac{\mathrm{i}}{2}\sqrt{4 - M^2} \\ \implies |\lambda_{1,2}| &= \sqrt{\frac{M^2}{4} + \frac{4 - M^2}{4}} \leq 1 \\ \iff M^2 - 4 \leq 0 &\implies -2 \leq M \leq 2. \end{aligned} \tag{C.5}$$

In other words, we have the condition

$$-2 \leq 2 + 2R^2\cos(\theta) - 2R^2 - 2\Delta t^2 V_i^n \leq 2. \tag{C.6}$$

As was done in B, we will analyze the cases where $M \leq 2$ and $M \geq -2$. When $M \leq 2$, we have

$$\begin{aligned} 2 + 2R^2\cos(\theta) - 2R^2 - 2\Delta t^2 V_i^n \leq 2 &\leq 2 + 2\Delta t^2 \tilde{V} \\ R^2\cos(\theta) - R^2 - \Delta t^2 V_i^n &\leq \Delta t^2 \tilde{V} \\ \frac{1}{\Delta x^2}(\cos(\theta) - 1) - V_i^n &\leq \tilde{V}, \end{aligned} \tag{C.7}$$

which will always be satisfied since $\tilde{V} > 0$ and $\cos(\theta) - 1 \leq 0$. Now, when $M \geq -2$ we have

$$\begin{aligned} -2 &\leq 2 + 2R^2\cos(\theta) - 2R^2 - 2\Delta t^2 V_i^n \\ -4 \leq 2R^2(\cos(\theta) - 1) - 2\Delta t^2 V_i^n &\leq -4R^2 - 2\Delta t^2 V_i^n \\ 4 &\geq 4R^2 + 2\Delta t^2 V_i^n. \end{aligned} \tag{C.8}$$

Since the above relation must hold for all V_i^n it must also hold true for $\tilde{V}$. Hence, we can

simplify the given expression by simply replacing $V_i^n \to \tilde{V}$. Hence,

$$\begin{aligned} 4 &\geq 4R^2 + 2\Delta t^2 \tilde{V} \\ 4 &\geq \Delta t^2 \left(\frac{4}{\Delta x^2} + 2\tilde{V} \right) \\ \implies \Delta t^2 &\leq \frac{2\Delta x^2}{2 + \tilde{V}}. \end{aligned} \tag{C.9}$$

We can clearly see the similarities between the CFL factor for the free wave equation and the wave equation in the presence of an external potential. In the case of an external potential, the size of the time step is inversely proportional to the height of the potential. As a result, running simulations with large potentials will require more memory in order to store the necessary data.

C.2 Derivation of the Trapezoidal Rule for Multiple Integrations

In order to derive the 2D trapezoidal rule discussed in 4.3, we first consider a smooth function $f(x, y)$ defined over a discrete domain with grid points $\{x_i\}_{i=1}^{N_x}$ and $\{y_j\}_{j=1}^{N_y}$ whose grid spacings are Δx and Δy, respectively. Then, we have

$$\int_{a_y}^{b_y} \int_{a_x}^{b_x} \mathrm{d}x\mathrm{d}y\, f(x, y) = \int_{a_y}^{b_y} \mathrm{d}y \left(\frac{\Delta x}{2} (\underbrace{f(x_0, y)}_{I_1} + \underbrace{f(x_{N_x}, y)}_{I_2}) + \underbrace{\Delta x \sum_{i=1}^{N_x - 1} f(x_i, y)}_{I_3} \right) \tag{C.10}$$

We now apply the trapezoidal rule over y to the result of our integration in x. We first compute I_1 as

$$\frac{\Delta x}{2} \int \mathrm{d}y f(x_0, y) = \frac{\Delta x \Delta y}{4} (f(x_0, y_0) + f(x_0, y_{N-y})) + \frac{\Delta x \Delta y}{2} \sum_{j=1}^{N_y - 1} f(x_0, y_j). \tag{C.11}$$

For I_2 we have

$$\frac{\Delta x}{2}\int \mathrm{d}y f(x_{N_x}, y) = \frac{\Delta x \Delta y}{4}(f(x_{N_x}, y_0) + f(x_{N_x}, y_{N-y})) + \frac{\Delta x \Delta y}{2}\sum_{j=1}^{N_y-1} f(x_{N_x}, y_j). \quad \text{(C.12)}$$

Finally, for I_3 we obtain

$$\begin{aligned}\Delta x \sum_{i=1}^{N_x-1}\int \mathrm{d}y f(x_i, y) = \frac{\Delta x \Delta y}{2}\sum_{i=1}^{N_x-1} f(x_i, y_0) + \frac{\Delta x \Delta y}{2}\sum_{i=1}^{N_x-1} f(x_i, y_{N_y}) \\ + \Delta x \Delta y \sum_{i=1}^{N_x-1}\sum_{j=1}^{N_y-1} f(x_i, y_j). \quad \text{(C.13)}\end{aligned}$$

From Eqs. (C.11),(C.12), and (C.13) we can clearly see three distinct "regions" in which we are calculating the integral. The first region is the corner points of our domain. Namely, $f(x_0, y_0)$. $f(x_0, y_{N_y})$, $f(x_{N_x}, y_0)$, and $f(x_{N_x}, y_{N_y})$ all of which obtain a weighting of $\frac{1}{4}$ as seen by the prefactors. Next, are the "edges" of the domain given by the points $f(x_0, y_j)$, $f(x_{N_x}, y_j)$, $f(x_i, y_0)$, and $f(x_i, y_{N_y})$, where $i \in [1, N_x - 1]$ and $j \in [1, N_y - 1]$, which obtain weights of $\frac{1}{2}$. Finally, we have the "interior" points given by $f(x_i, y_j)$ for $i \in [1, N_x - 1]$ and $j \in [1, N_y - 1]$ which have weights of 1. In order to numerically integrate 2D functions, such as the ones in Sec. 4.3, one must ensure that each of these regions is handled appropriately.